SAND REPORT

SAND2003-0954
Unlimited Release
Printed March 2003

Design and Testing of a Micro Thermal Conductivity Detector (TCD) System

Steven K. Showalter, Dolores Cruz, Fred Gelbard, Ronald P. Manginell, Douglas R. Adkins, Richard Kottenstette, K. Scott Rawlinson, George R. Dulleck Jr., Daniel S. Horschel and Wayne Einfeld

Prepared by
Sandia National Laboratories
Albuquerque, New Mexico 87185 and Livermore, California 94550

Sandia is a multiprogram laboratory operated by Sandia Corporation,
a Lockheed Martin Company, for the United States Department of Energy's
National Nuclear Security Administration under Contract DE-AC04-94-AL85000.

Approved for public release; further dissemination unlimited.

Sandia National Laboratories

Issued by Sandia National Laboratories, operated for the United States Department of Energy by Sandia Corporation.

NOTICE: This report was prepared as an account of work sponsored by an agency of the United States Government. Neither the United States Government, nor any agency thereof, nor any of their employees, nor any of their contractors, subcontractors, or their employees, make any warranty, express or implied, or assume any legal liability or responsibility for the accuracy, completeness, or usefulness of any information, apparatus, product, or process disclosed, or represent that its use would not infringe privately owned rights. Reference herein to any specific commercial product, process, or service by trade name, trademark, manufacturer, or otherwise, does not necessarily constitute or imply its endorsement, recommendation, or favoring by the United States Government, any agency thereof, or any of their contractors or subcontractors. The views and opinions expressed herein do not necessarily state or reflect those of the United States Government, any agency thereof, or any of their contractors.

Printed in the United States of America. This report has been reproduced directly from the best available copy.

Available to DOE and DOE contractors from
U.S. Department of Energy
Office of Scientific and Technical Information
P.O. Box 62
Oak Ridge, TN 37831

Telephone: (865)576-8401
Facsimile: (865)576-5728
E-Mail: reports@adonis.osti.gov
Online ordering: http://www.doe.gov/bridge

Available to the public from
U.S. Department of Commerce
National Technical Information Service
5285 Port Royal Rd
Springfield, VA 22161

Telephone: (800)553-6847
Facsimile: (703)605-6900
E-Mail: orders@ntis.fedworld.gov
Online order: http://www.ntis.gov/help/ordermethods.asp?loc=7-4-0#online

SAND2003-0954
Unlimited Release
Printed March 2004

Design and Testing of a Micro Thermal Conductivity Detector (TCD) System

Steven K. Showalter, Dolores Cruz, Ronald P. Manginell,
Douglas R. Adkins and Richard Kottenstette
Micro-Total-Analytical Systems Department

Fred Gelbard
Modeling and Analysis Department

George R. Dulleck Jr.
Integrated Microsystems Department

K. Scott Rawlinson
Solar Technologies Department

Daniel S. Horschel and Wayne Einfeld
Environmental Monitoring and Characterization Department

Sandia National Laboratories
P.O. Box 5800
Albuquerque, NM 87185-0892

Abstract

This work describes the design, simulation, fabrication and characterization of a microfabricated thermal conductivity detector to be used as an extension of the µChemLab™. The device geometry was optimized by simulating the heat transfer in the device, utilizing a boundary element algorithm. In particular it is shown that within microfabrication constraints, a micro-TCD optimized for sensitivity can be readily calculated. Two flow patterns were proposed and were subsequently fabricated into nine-promising geometries. The microfabricated detector consists of a slender metal film, supported by a suspended thin dielectric film over a pyramidal or trapezoidal silicon channel. It was demonstrated that the perpendicular flow, where the gas directly impinges on the membrane, creates a device that is 3 times more sensitive than the parallel flow, where the gas passes over the membrane. This resulted in validation of the functionality of a microfabricated TCD as a trace-level detector, utilizing low power. The detector shows a consistent linear response to concentration and we are easily able to detect 100-ppm levels of CO in He. Comparison of noise levels for this analysis indicates that sub part per million (ppm) levels are achievable with the selection of the right set of conditions for the detector to operate under. This detector was originally proposed as part of a high-speed detection system for the petrochemical gas industry. This system was to be utilized as a process monitor to detect reactor “upset” conditions before a run away condition could occur (faster than current full-scale monitoring systems were able to achieve). Further outlining of requirements indicted that the detection levels likely achievable with a TCD detector would not be sufficient to meet the process condition needs. Therefore the designed and fabricated detector was integrated into a detection system to showcase some technologies that could further the development of components for the current gas phase µChemLab as well as future modifications for process monitoring work such as: pressurized connections, gas sampling procedures, packed columns. Component integration of a microfabricated planar pre-concentrator, gas-chromatograph column and TCD in the separation/detection of hydrocarbons, such as benzene, toluene and xylene (BTX) was also demonstrated with this system.

(This page intentionally left blank).

TABLE OF CONTENTS

ABSTRACT **3**
LIST OF FIGURES **6**
LIST OF TABLES **8**
INTRODUCTION **9**
TCD DESIGN **10**
THEORETICAL ANALYSIS **15**
Governing Heat Transfer Mechanism 15
COMPUTATIONAL RESULTS **17**
FABRICATION **22**
BENCH SCALE EXPERIMENTAL RESULTS **27**
SYSTEM INTEGRATION **33**
Background 33
System Design 35
Fluidic Interconnects Updates 36
Sampling System 37
Novel Columns 39
Detector Packaging 40
Electronic Controls 41
Completed System 43
DISCUSSION **44**
CONCLUSIONS **47**
Definitions 49
APPENDIX A: BOUNDARY ELEMENT FORMULATION AND SOLUTION OF LAPLACE'S EQUATION **50**
APPENDIX B: PROCESS FLOW SHEET FOR MICROTCD **62**
110_FIND Mask 62
FINDING THE 110 PLANE 63
METAL 1 MASK 66
METAL 2 MASK 67
KOH Mask 68
REFERENCES **73**

List of Figures

Figure 1. Wheatstone bridge circuitry for TCD. A zero voltage will be indicated if $R_1R_4 = R_2R_3$ (A). Bridge circuit used in a four-cell detector (B). This method gives twice the response than the circuit shown (A). 11
Figure 2. Side view of channel. The slanted sidewalls are at 54.74 degrees from the horizontal and are assumed to be at a constant ambient temperature. The heater and nitride layers are shown in red and blue, respectively, and are approximately 1.5 and 1 μm thick, respectively. The slanted sidewalls may be truncated at the bottom to allow gas flow upwards through the device. The truncated regions of the sidewalls are shown as dashed lines. This diagram is invariant to 90-degree rotations about the vertical axis from the center of the heater. 12
Figure 3. Top view of channel. Trapezoidal openings, where the silicon will be etched, are patterned on the nitride layer to form the suspended membrane. A meandered heater wire is deposited on top of the square region of the nitride membrane. This square has dimensions of L by L as shown in Figure 3. The wire leads to the heater run along the center of two of the nitride legs. (These legs are not shown in the side view given in Figure 3.) 13
Figure 4. Trapezoidal channel with depth (D) equal to the thickness of the wafer. 13
Figure 5. Gas introduction perpendicular to the membrane (A). In this case the gas escapes through the top openings of the channel. Gas introduction parallel to the membrane (B). The arrows indicate the direction of gas flow. 14
Figure 6. Three-dimensional view of temperature profile in TCD. 18
Figure 7. Temperature Profile in TCD. This cell has dimensions of L=500 μm and C = 500 μm. The heater is kept at 75˚ C and the sidewalls at 50 ˚C. The gas used is helium with a thermal conductivity of 1.57 x 10^{-4} mW/μm-K. 18
Figure 8. Top view of temperature profile in TCD. This cell has dimensions of L=500 μm and C=500 μm. In this figure only two of the legs are heated. 19
Figure 9. Q vs. k for a 100 μm membrane held at constant temperature of 75 ˚C and various opening sizes. dQ/dk increases as the opening increase. 20
Figure 10. Q vs. k for a membrane with dimensions of L=200 μm and various C. The heater is held at a constant temperature of 75 ˚C. dQ/dk increases as the opening increases. 20
Figure 11. Q vs. k for a membrane with dimensions of L=200 μm and various C. The heater is held at a constant temperature of 100° C. dQ/dk increases as the opening increase. 21
Figure 12. Q vs. k for a membrane with dimensions of L=500 μm and various C. The heater is held at a constant temperature of 100 ˚C. dQ/dk increases as the opening increases. 22
Figure 13. LPCVD silicon nitride wafer. Because the nitride serves as a hard-mask for the KOH etch, it must be deposited on both sides of the wafer. 23
Figure 14. Silicon Nitride wafer with sputtered chromium adhesion layer (200 A) and platinum resistor (5000 A). 23
Figure 15. Patterned nitride, top (top) and cross sectional views (bottom). The nitride serves as a hard mask for the KOH etch. 24

Figure 16. Anisotropically etched silicon wafer. Plane directions are shown. In this case, the wafer has been etched through. 24
Figure 17. SEM image of micro-TCD cross-section. Suspended membrane remains standing after being diced in half showing its low stress. 25
Figure 18. Deposited and patterned resistor on suspended silicon membrane. 25
Figure 19. Deposited and patterned gold bond pad, 1 μm thick with 200 Å layer of chromium for adhesion... 25
Figure 20 Wire-bonded part ready for fluidic connections (left) and completed part (right) ready for testing. 26
Figure 21. Pyrex Lids and how they fit over device to accomplish perpendicular flow and parallel flow. There are two sizes to fit over the different sized TCDs. Restricting the flow path as narrowly as possible increases the sensitivity of the TCD in the perpendicular flow scheme. 27
Figure 22 Wiring diagrams for 24-pin DIP pin out for Parallel, Perpendicular and Dual TCD styles. Resistance varied from device to device so 1k was used as a placeholder. The starting resistance is not overly significant since this is a bridge circuit and as long as all resistances are equal the bridge will be balanced. 28
Figure 23. Experimental test set up for detector testing. 29
Figure 24. Time response of TCD for different concentrations of air (left). The carrier gas is He at 5sccm, the TCD is a membrane of 500μm with an etch opening of 100μm. The voltage is 5V (100 ^{o}C). Detector linear response. The peaks were integrated to assess the response. (right) 30
Figure 25. Time response for TCD for various concentrations of air. Detector used has a membrane size of 300 μm and an etch opening of 100 μm. He is used as the carrier gas and flowed at 5 sccm. (A) Close up of first peak tail from 30 seconds to 38 seconds. The tail is shallow and has a sharp drop (B). Close up of third peak's tail from 100 seconds to 140 seconds. (C) 31
Figure 26. Time response for toluene/air mixture. Device is configured in perpendicular flow and dimensions are L=300 μm, C=100 μm, temperature is 300 ^{o}C. (A). Linear response of device to air and toluene/air mixture at various concentrations (B). 31
Figure 27. Experimental results and simulation. The device is a membrane with length of 500 μm and an etch opening of 100 μm. However, both resistors are suspended on the membrane (dual configuration). 32
Figure 28 Microfabricated GC column (left) and preconcentrator. Nickel is included for size comparison. 34
Figure 29 TCD System schematic drawing 35
Figure 30 Commercial NanoPort fittings with Teflon tubing.. 36
Figure 31 Dual meso-valves used for sample introduction and analysis train isolation, mounted on backside of system box. 37
Figure 32 Miniature diaphragm pump used to load PCs 38
Figure 33 Design diagram of PC holder showing the lid and body with space for O-ring seal. The dark square in the center of the body is where the PC sits. Opening at base is for NanoPort^{TM} connection that flows into square and out other side. This connects to another NanoPort^{TM} on other side of part (hidden from view). Electrical contacts are made with the PC through the lid via pogo pins.................................... 38

Figure 34 Completely assembled GC column packed with modified NanoPort female fittings and molecular sieve adsorbent. Wires on the right are thermistor leads; wires on the left are column heater leads. 40
Figure 35 Diagram of lid for TCD in transparent rendering to show NanoPort connections and face match with Pyrex lid........ 41
Figure 37 Complete system. PCs are in the numbered cylinders on the right side of box, TCD is at the center, the column is suspended to the lower right and LCD output display is at lower left. 43
Figure 38. Time response of μTCD for 100-ppm CO in He. Device is configured in perpendicular flow; dimensions are membrane 500 μm and etch opening of 100 μm. This is data from the bench scale testing, not the system test. He is used as the carrier gas and flow is 5sccm. 44
Figure 39 Data from system showing two output channels used for collection. The signal is inverted because the bridge and reference had to be switched to allow the differential output across the bridge to remain within the range of the A-D converters. Channel B and D output, which is overlaid illustrating firing of a single preconcentrator loaded with benzene, toluene and xylene. 45
Figure 40 Thermistor output data from system during typical run. Notice that the variance is about 80 ticks whereas for the data in above figure has a differential of near 400 ticks, peak to baseline. 46
Figure 41 Data channels B and D again. This is toluene fired off three preconcentrators. Two PC pulses appear to have combined with a third PC pulse lagging. 46
Figure 42. Detection of benzene, toluene and xylene eluted from μGC. TCD detector is membrane 300 μm and etch opening of 100 μm. 48

List of Tables

Table 1. Properties of metals used. [CRC handbook] 23
Table 2 Selected gases and their thermal conductivities at room temperature. 28
Table 3. Design of Experiment Matrix. 33

Introduction

A thermal conductivity detector (TCD) is a simple and robust device for measuring deviations in the thermal conductivity of a gas. Conventional TCDs are simple, robust and universally used with gas-chromatograph columns [Grob, 1995]. When used to analyze the effluent from a gas chromatography column (GC), the presence of eluted gases such as CS_2, COS, H_2S, SO_2, CO, NO, NO_2 and CO_2 can be determined from the variations of thermal conductivity of the carrier gas.

Conventional TCDs consist of a heated thin metallic coiled filament, which is approximately 2 cm in length and runs axially along an unheated cylindrical stainless steel body. The cylindrical sample volume is in the order of 0.5 cm^3. We propose the miniaturization of the TCDs by reducing the sample volume by four orders of magnitude. Scaling down the TCD volume does not affect the gas concentration (concentration detector not a mass detector). This makes the TCD a great candidate for miniaturization. Moreover, a TCD can be integrated with a micro-gas chromatography column to form a complete "lab-on-a-chip" separation-detection scheme, or a so called "micro-Total Analytical System (μTAS)". This would enhance the current sensor system, which presently utilizes a surface acoustic wave (SAW) detector. The TCD will augment the types of gases that can be identified because it is a nondestructive detector similar to the SAW.

Currently, there are commercially available micro-TCDs, such as the one developed by Varian [www.varian.com]. Yet, their detector and column operates at a fixed temperature of 110°C, not utilizing the ability of micro-resistors to heat up to temperatures of 500°C in a matter of seconds. Moreover, micro machining provides ease of bulk fabrication, reduction of costs and uniformity across devices [Kovacs, 1998, p 1]. Fabrication on silicon substrates of the TCDs allows versatility in design and integration with other microfabricated components, such as a microfabricated gas-chromatograph column. In the past, microfabricated TCDs have been investigated [Kimura, Muto, Simon, Sittleler, Sorge, Wu]. However, there seems to be limited work on optimizing the geometry of TCDs for greatest sensitivity to trace quantities of eluted gases. Motivated by this need, we demonstrate in this work the cost effectiveness of computational prototyping of μTCDs. Such systems can of course be designed by the well-established laboratory approach of "trial and (much) error". However, as shown in this work, fully three-dimensional simulations of detector sensitivity for hundreds or even thousands of different designs can be assessed on a personal computer in a matter of hours. Thus, time and money can be saved by computational prototyping. In particular, we show that within microfabrication constraints, a micro TCD optimized for sensitivity can be readily modeled.

This work begins with a discussion of the TCD design and available degrees of freedom. Within fabrication constraints, there are three degrees of freedom in terms of the proposed device dimensions. We discuss the dominating modes of heat transfer in the body of the TCD and how they are modeled in the simulation. This work will discuss computational results and indicate which geometry can demonstrate the greatest sensitivity. We also recommend an efficient and straightforward method of fabrication.

This detector was originally proposed as part of a high-speed, nonflame based detection system for the petrochemical gas industry. The system was to be utilized as a process monitor to detect reactor “upset” conditions before a run away condition could occur (faster than current full-scale monitoring systems were able to achieve). Further outlining of requirements indicted that the detection levels likely achievable with a TCD detector would not be sufficient to meet the process condition needs. Therefore the designed and fabricated detector was integrated into a detection system to showcase some technologies that could further the development of components for the current gas phase µChemLab as well as future modifications for process monitoring work such as: pressurized connections, gas sampling procedures, packed columns. We have demonstrated the functionality of the TCD and its integration with other microfabricated components. Various upgrades to the system have been developed that may have utility in future designs of the µChemLab system such as make-and-break fluidic pressurized connections, flexible tubing, microvalved sampling, use of a pressurized carrier gas, packed micro GC columns and the use of multiple PCs to increase sample loading as well as the range of captured analytes.

TCD Design

A typical arrangement for a TCD is shown in Figure 1. In this Whetstone bridge circuit, a constant current I is applied at the top of the bridge and flows to ground through both the left path of R_1 and R_3, and the right path of R_2 and R_4. The bridge is balanced, (i.e. a zero voltage will be obtained), if the resistances are such that $R_1R_4 = R_2R_3$. Thus, if by design R_1 and R_2 are equal, then a nonzero voltage measurement will be obtained only when $R_4 \neq R_3$. If also the flow cells that determine resistances R_3 and R_4 are identical, these resistances will differ only if the gases in the flow cells differ.

Figure 1. Wheatstone bridge circuitry for TCD. A zero voltage will be indicated if $R_1R_4 = R_2R_3$ (A). Bridge circuit used in a four-cell detector (B). This method gives twice the response than the circuit shown (A).

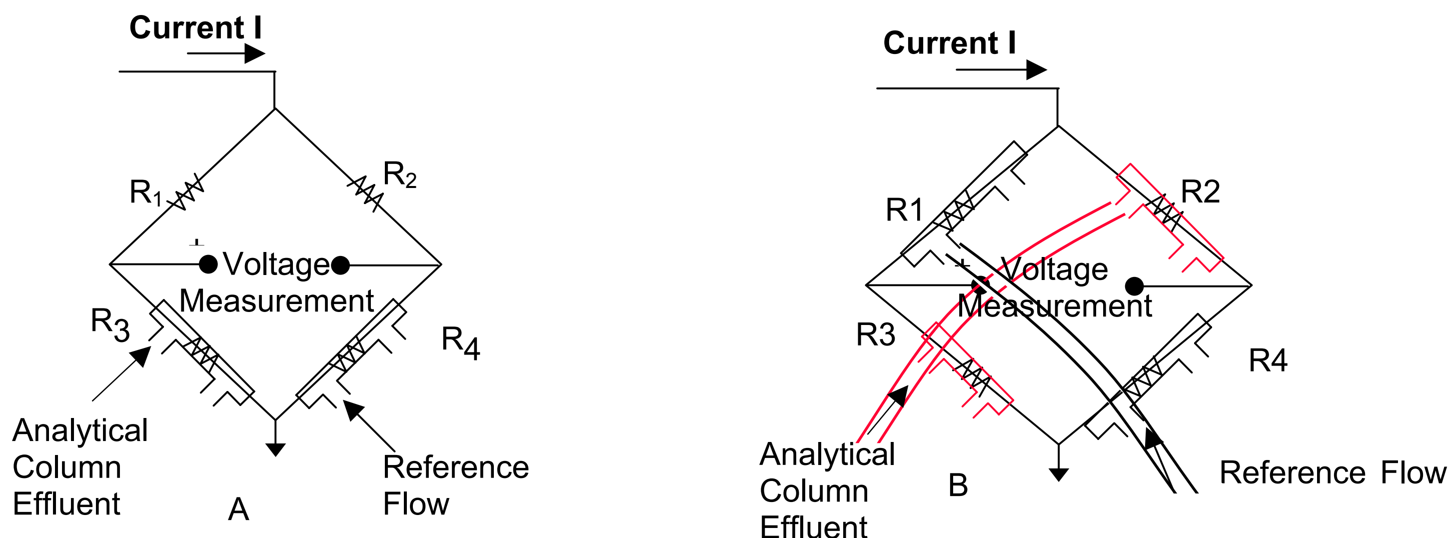

Figure 1 (B) shows another configuration of the bridge circuit, which replaces resistors R_1 and R_2 with two more filament cells. The effluent from the analytical column is split into corresponding cells of resistance R_3. The effluent from the reference column is sent to two corresponding cells of resistance R_4. This configuration yields a doubling in the response factor since two cells are contributing to the change in signal. An important component not shown in the bridge circuit is a variable resistor. The variable resistor is connected in series to one leg of the bridge to zero the voltage, under background flow conditions, before a chromatogram is run.

A proposed micro flow cell is shown schematically from side and top views in Figures 2 and 3, respectively. The meandered heating element rests on a silicon nitride (Si_xN_y) membrane. Because of the thinness of the nitride membrane, the square region of nitride is assumed to be at the same temperature as the heater. If a metal whose resistance, R_f, is temperature dependent is used for the heater, the temperature of the heater can be inferred from determining the resistance and using Equation (1).

$$R_f = R_f^o(1 + \alpha_T T_f) \quad (1)$$

where α_T is the temperature coefficient of resistance, R_f^o is the electrical resistivity of the filament at a reference condition and T_f is the temperature of the filament, in our case the heater. For detection it is the change in thermal conductivity, k that is important.

This change, caused by the presence of an eluted gas, will change the temperature of the heater, changing its resistance, according to

$$\Delta R_f = \alpha_T R_f^o \Delta T_f \,. \quad (2)$$

The change in temperature is given by,

$$\Delta T_f = \frac{T_f - T_c}{k} \Delta k \quad (3)$$

where T_c is the temperature of the channel. Combining Equations (2) and (3), we get the change in resistance with respect to thermal conductivity as

$$\Delta R_f = \frac{-\alpha_T R_f^o (T_f - T_c) \Delta k}{k} \,. \quad (4)$$

Therefore, if we measure the voltage across the bridge and determine the resistance using Ohm's law, we can determine the resistance and the change in resistance, leading to the change in thermal conductivity. The sensitivity of the μTCD to these changes is dependent on its geometry. We propose the fabrication of the TCD using a silicon substrate and an anisotropic wet etchant, potassium hydroxide (KOH). The channel size is defined by the opening where the KOH etches the silicon, defining a pyramidal-like structure with a suspended membrane in Figure 2. The etching is such that the slanted sidewalls are at 54.74 degrees from the horizontal in Figure 2. These sidewalls are maintained at an ambient temperature of 25° C. The opening and the membrane size determine the depth of the channel.

Figure 2. Side view of channel. The slanted sidewalls are at 54.74 degrees from the horizontal and are assumed to be at a constant ambient temperature. The heater and nitride layers are shown in red and blue, respectively, and are approximately 1.5 and 1 μm thick, respectively. The slanted sidewalls may be truncated at the bottom to allow gas flow upwards through the device. The truncated regions of the sidewalls are shown as dashed lines. This diagram is invariant to 90-degree rotations about the vertical axis from the center of the heater.

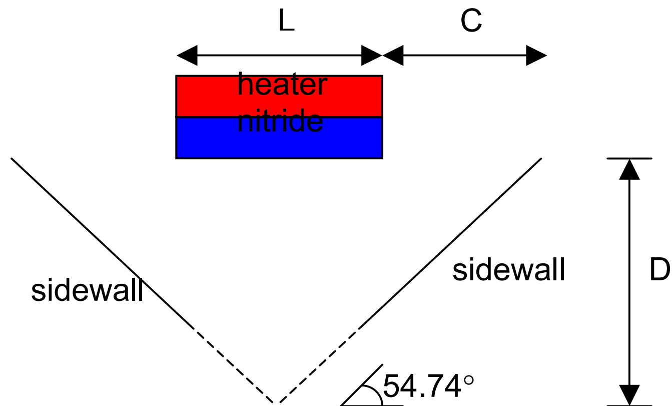

Figure 3. Top view of channel. Trapezoidal openings, where the silicon will be etched, are patterned on the nitride layer to form the suspended membrane. A meandered heater wire is deposited on top of the square region of the nitride membrane. This square has dimensions of L by L as shown in Figure 3. The wire leads to the heater run along the center of two of the nitride legs. (These legs are not shown in the side view given in Figure 3.)

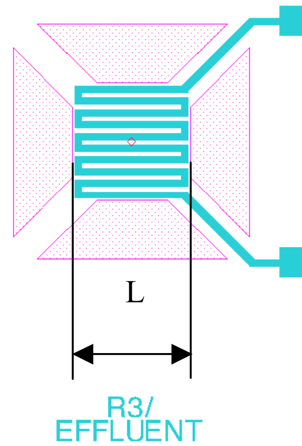

A designer may vary the heater temperature and the geometry by varying D, L, and C, the channel depth, heater size, and channel width, respectively. However, these degrees of freedom have constraints. The channel depth cannot be deeper than the thickness of the silicon wafer, which is typically $D_{wafer} \leq 350$ to $500\ \mu m$. Therefore,

$$500\ \mu\text{m} > D = \left(C + \frac{L}{2}\right)\tan(54.74^\circ)\ . \tag{5}$$

If D is greater than 500 µm, the channel will be truncated and it will form a trapezoidal channel. Figure 4 depicts the newly formed channel when the calculated depth using Equation (1) is greater than the wafer thickness.

Figure 4. Trapezoidal channel with depth (D) equal to the thickness of the wafer.

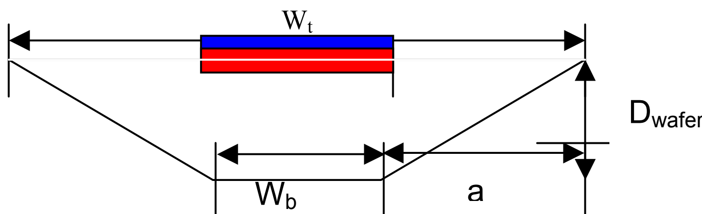

The dimensions of the truncated channel are as follows:

$$W_t = L + 2C = W_b + 2a \tag{6}$$

$$a = \frac{D}{\tan(54.74^o)} \qquad (7)$$

It follows then that the width of the bottom opening is defined by,

$$W_b = L + 2C - \frac{2D}{\tan(54.74^o)} \qquad (8)$$

Therefore, there are two channel shapes that can be microfabricated using anisotropic etching of silicon. A pyramidal channel, whose geometry is constrained by Equation (1) and a trapezoidal channel whose depth equals the wafer thickness and openings are defined by Equations (5) and (7). Despite these constraints, there is much latitude in specifying the geometry and operating temperature. For this work we consider five heater sizes from L = 100 to 500 μm in increments of 100 μm, five channel widths from C = 100 to 500 μm in increments of 100 μm, and six heater temperatures from 75 to 200 C in increments of 25 C. This represents a total of (6)(5)(5) = 150 different geometric configurations. For each configuration, seven thermal conductivities, ranging from 10^{-5} to 4×10^{-4} mW/μm/K were considered. Thus, a total of (7)(150) = 1050 simulations were performed to determine the optimum configuration and operating temperature. There are a total of twenty-five different channel sizes. Of these twenty-five, nine geometries form a pyramidal channel and sixteen geometries form a trapezoidal channel. All twenty-five geometries were analyzed at six different temperatures and seven thermal conductivities.

The design of the microfabricated TCD allows two methods of gas introduction, as seen in Figure 5. Gas can be introduced either perpendicular, as shown in Figure 5(A), or parallel to the membrane, as shown in Figure 5 (B). When the gas is introduced perpendicularly through the bottom of the channel it escapes through the top. (The top being the location of the suspended membrane.) For the parallel gas introduction, a lid must cap the channel to ensure impingement on the membrane.

Figure 5. Gas introduction perpendicular to the membrane (A). In this case the gas escapes through the top openings of the channel. Gas introduction parallel to the membrane (B). The arrows indicate the direction of gas flow.

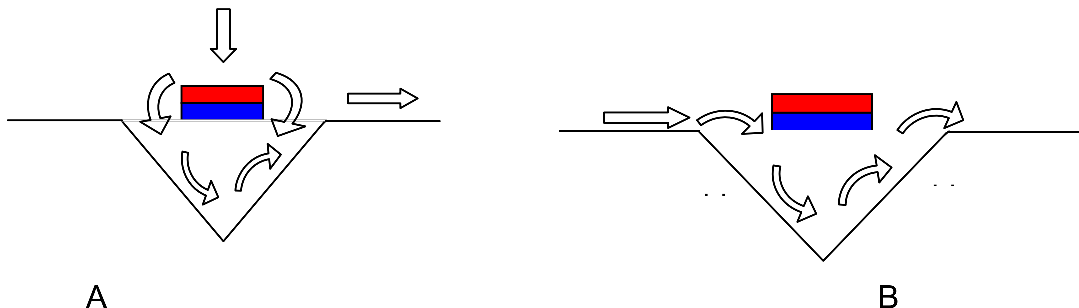

The optimum design has the greatest sensitivity to changes in gas thermal conductivity. This corresponds to a design for which Q, the heat flux from the heater is most sensitive to variations in k, the thermal conductivity. Thus, we seek the geometry for which dQ/dk is maximized.

Theoretical Analysis

Governing Heat Transfer Mechanism

The three modes for heat transfer from the heater to the sidewalls are conduction through the gas, convective heat transfer by the flowing gas, and radiation through the gas. We will now show that for the geometries and flow conditions, convection and conduction dominate over radiation.

The ratio of convective to conductive heat transfer is given by the Peclet number, which is defined as

$$Pe \equiv \frac{vL}{\alpha} \qquad (9)$$

where v and L are the characteristic gas velocities and channel size. The thermal diffusivity of the gas is defined as

$$\alpha \equiv \frac{k}{\rho Cp} \qquad (10)$$

where k, ρ, and Cp, are the gas thermal conductivity, density, and constant pressure heat capacity, respectively. A flow rate of 1 mL/sec = 10^{-6} m^3/s is typical of the flow rate through a micro GC. The highest flow velocity would be for the smallest value of C = 100 μm, which results in an effluent cross-sectional area of approximately 8×10^{-8} m^2. For helium at 93 ºC, $\alpha = 2.5 \times 10^{-4}$ m^2/s. Thus, for a characteristic length of 100 μm = 10^{-4} m

$$Pe = (10^{-6}\ m^3/s)(10^{-4}\ m)/[(8 \times 10^{-8}\ m^2)(2.5 \times 10^{-4}\ m^2/s)] = 5 \qquad (11)$$

Because the Peclet number is greater than one, convection dominates over conduction.

Now, we will show that radiative heat transfer is orders of magnitude smaller than conductive heat transfer. The governing equation for radiation heat transfer between two non-black bodies i and j is

$$Q = \varepsilon_i \sigma A_i F_{ij} (T_i^4 - T_j^4) \qquad (12)$$

where ε_i is the emissivity of the material, σ is the Stefan-Boltzman constant = 5.67051 × 10^{-8} W/m^2/K^4, A_i is the total area of body i and F_{ij} is the view factor. For our calculations we assumed the view factor to be 1 (its greatest possible value). Consider the greatest temperature difference T_1 = 200 C and T_2 = 25 C from the simulation, and the greatest area of the membrane (A_1 = 250000 μm^2). Therefore, for silicon nitride, whose total normal emittance is 0.9,

$$Q = 0.9(5.67051 \times 10^{-8}\ W/m^2/K^4)(2.5 \times 10^{-7}\ m^2)(1)(473^4\ K^4 - 298^4\ K^4) = 5.4 \times 10^{-4}\ W \qquad (13)$$

Preliminary simulation results indicated that the heat transfer due to conduction is on the order of approximately 50 mW, approximately 2 orders of magnitude greater than that of radiation. We performed similar calculations for the metal (platinum) and silicon. These yielded comparable results, indicating radiation heat transfer is negligible compared to conduction.

Unfortunately the codes that were developed only addressed conduction and ignored convection as well as radiation effects. This allowed a much simpler code to be run and for a large number of potential devices to be tested. Unfortunately modeling trends may not apply to the actual physical devices. Enough information was obtained from the simple modeling results to allow the fabrication of a set of devices, which could then be tested alongside one another to see if ignoring the convective or radiation effects was indeed valid for the heat transfer in this system.

Governing Equation for Heat Transfer
In the pyramidal or trapezoidal chamber that encloses the gas, the governing equation for steady heat conduction is given by Laplace's equation,

$$\nabla^2 T = 0 \tag{14}$$

where T is the temperature and ∇^2 is the Laplacian. The boundary conditions are T = 25° C on the sidewalls, zero heat flux where the gas enters and leaves the chamber, and the heater temperature varies from 75° to 200° C. A solution to Eq. (13) with these boundary conditions provides the temperature as a function of spatial position in the chamber. Then the heat flux out of the heater is given by

$$Q = -k \int_{\text{heater area}} \nabla T \bullet \vec{n} \, ds \tag{15}$$

where $\vec{n}$ is the outer normal from the heater into the gaseous region of the chamber, ∇T is the temperature gradient, and ds is the differential heater surface area. dQ/dk is determined from the two values of Q at two different values of k. Notice that to determine Q, the temperature need not be determined throughout the chamber. Only ∇T is needed at the surface of the heater to determine Q. In general, spatial discretization algorithms such as finite elements, finite volume, and finite difference would involve solving for the temperature field throughout the chamber, and then determining ∇T at the heater surface to determine Q. However, it is far more computationally efficient to solve only for ∇T at the heater surface by using a Boundary Element Method. This is the algorithm used in this work and is discussed in detail in the Appendix.

Computational Results
The simulation of the heat flux in the TCD for over a thousand configurations was run on a Dell Optiplex Gx150 Pentium III 1.13GHz 512MB SDRAM personal computer in a matter of hours. The simulation results are plotted in two formats. The first format is a three dimensional representation of the temperature profile in the TCD. This illustrates the heat dissipation in the detector. Figure 6 shows a three-dimensional view of the temperature profile in the TCD. Figure 7 depicts the temperature profile in the TCD, which has been sliced through the x=0 plane. shows a top view of the same geometry. Figure 8.

Figure 6. Three-dimensional view of temperature profile in TCD.

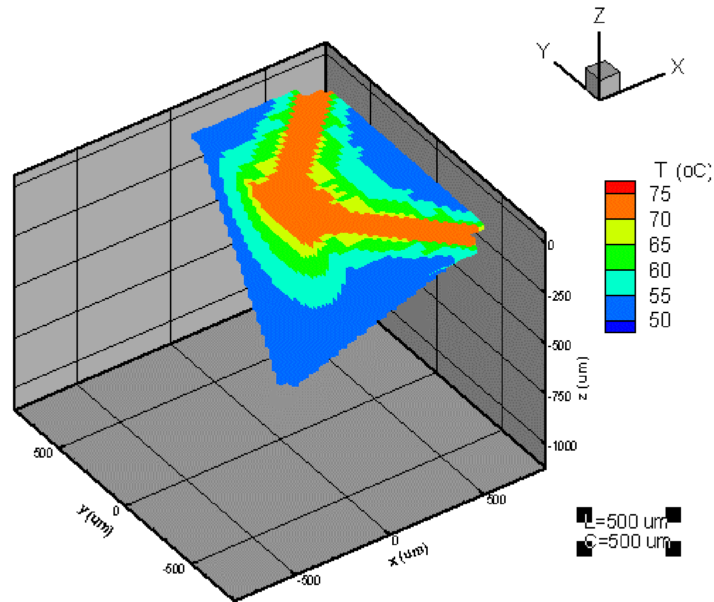

Figure 7. Temperature Profile in TCD. This cell has dimensions of L=500 μm and C = 500 μm. The heater is kept at 75˚ C and the sidewalls at 50 ˚C. The gas used is helium with a thermal conductivity of 1.57 x 10^{-4} mW/μm-K.

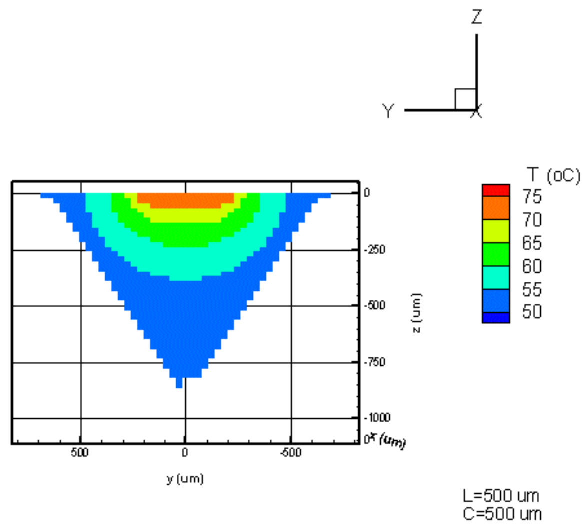

Figure 8. Top view of temperature profile in TCD. This cell has dimensions of L=500 μm and C=500 μm. In this figure only two of the legs are heated.

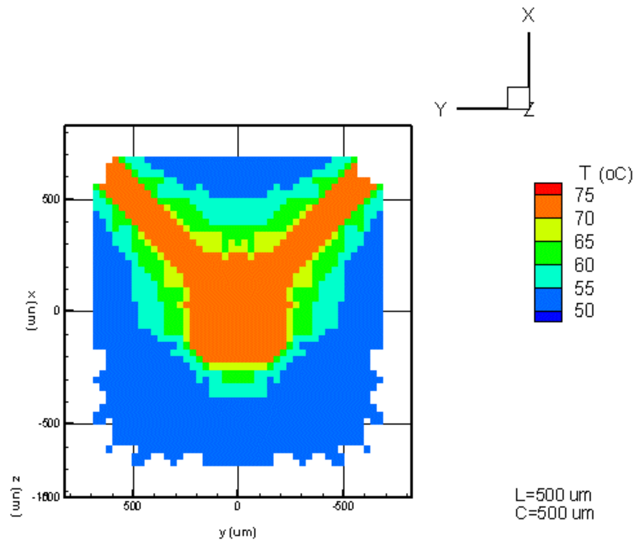

The second plotting format illustrates the change in heat flow versus gas thermal conductivity, which is the parameter of most interest. These are graphs of Q versus k. In this manner the change in heat flow versus the change in gas thermal conductivity ($\frac{dQ}{dk}$) can be assessed. The relationship between Q and k is linear for a fixed geometry. Therefore, $\frac{dQ}{dk}$ will be constant and equal to the slope of a line of Q versus k for a given geometry. The results shown below in Figure 9 are for a nitride membrane that is a 100 × 100 μm square on to which the heater is placed. The nitride membrane that includes the four legs protruding from the corner of the square is maintained at 75 ˚C, and the sidewall temperature is 25 ˚C. Plotted is the heat flow from the heater versus gas thermal conductivity for five different openings. Thus, using the nomenclature in Figure 3, L = 100 μm, and C = 100, 200, 300, 400, or 500 μm. The most sensitive geometry demonstrates the greatest change in heat flow versus thermal conductivity. It is that geometry with the largest slope in Figure 9. It is clear that a value of C = 500 μm is the best design for this fixed heater size. Lines were fit to the data points using Origin Pro v. 6.1. A channel with L=100 μm and C=500 μm has a depth of approximately 630 μm. This is greater than the standard wafer thickness of 500 μm. Therefore, we must consider a trapezoidal channel with depth of 500 μm and same membrane and opening sizes. For a trapezoidal channel with these dimension dQ/dk = 4.13 x 10^{-4}, for the pyramidal channel dQ/dk = 4.12x 10^{-4}. It is interesting to note that trapezoidal channels give slightly better sensitivities than pyramidal channels for a given membrane and opening size.

Figure 9. Q vs. k for a 100 µm membrane held at constant temperature of 75 ˚C and various opening sizes. dQ/dk increases as the opening increase.

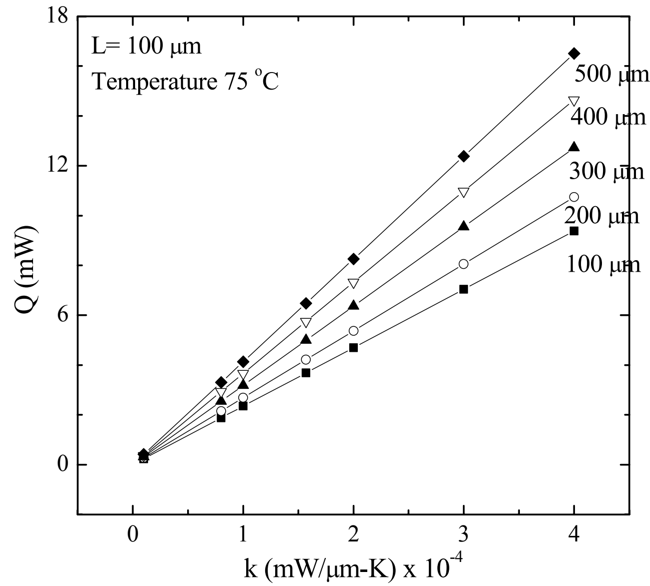

Figure 10 depicts the heat flow versus thermal conductivity for a membrane that has dimensions of 200 µm x 200 µm. There are five different opening sizes, C = 100, 200, 300, 400, and 500 µm. Once again the most sensitive geometry has the greatest slope that is the greatest change in heat flow with respect to thermal conductivity.

Figure 10. Q vs. k for a membrane with dimensions of L=200 µm and various C. The heater is held at a constant temperature of 75 ˚C. dQ/dk increases as the opening increases.

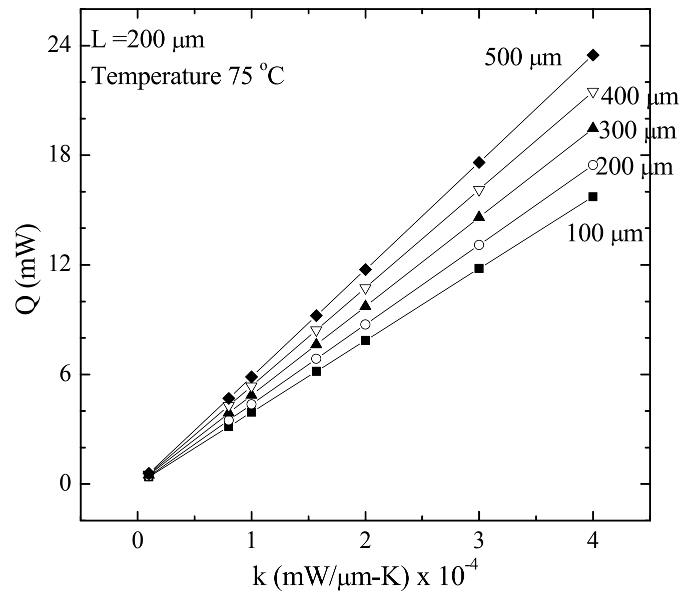

The results indicate that a bigger geometry gives you a larger $\frac{dQ}{dk}$. Also operating the resistor at a higher temperature will yield higher sensitivity in the detector. For example for a membrane with dimensions of L = 200 μm and C = 100 μm at 75 ˚C the sensitivity for the detector is $\frac{dQ}{dk}$ = 2.35 x 10^{-4} μm-K. For a membrane with the same dimensions, but at a temperature of 100 ˚C, the sensitivity is $\frac{dQ}{dk}$ = 4.70 x 10^{-4} μm-K. This is a doubling of the sensitivity for an increase of 7 % in absolute temperature (Figure 11).

Figure 11. Q vs. k for a membrane with dimensions of L=200 μm and various C. The heater is held at a constant temperature of 100° C. dQ/dk increases as the opening increase.

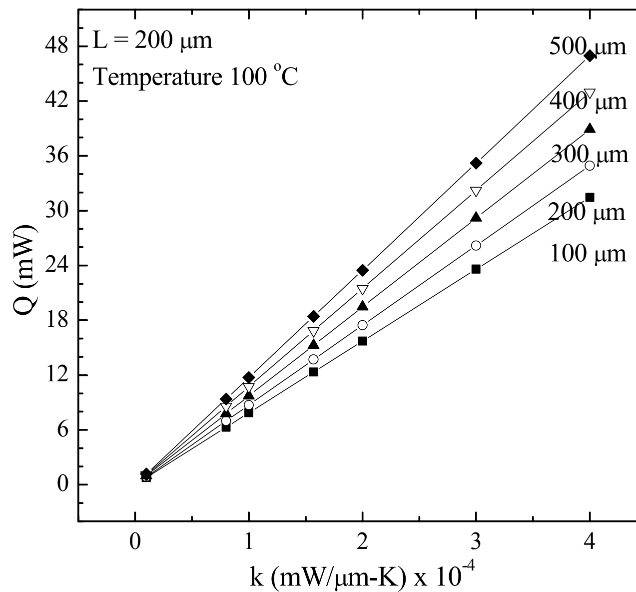

When the membrane has dimension of L = 500 μm and is at 100 ˚C, the opening size does not make a significant improvement in the sensitivity of the detector (Figure 12). The slopes of the lines range from dQ/dk = 19.6 × 10^{-4} μm-K to 21.8 × 10^{-4} μm-K (only a 10 % improvement). Compared to the L = 100 μm membrane when the slope of the lines ranged from dQ/dk = 4.8 × 10^{-4} μm-K to 8.3 × 10^{-4} μm-K (nearly a 100% improvement). However, the L = 500 μm membrane still provides the greatest sensitivity; this is due to the heat conduction and that greater thermal gradients can be sustained.

Figure 12. Q vs. k for a membrane with dimensions of L=500 μm and various C. The heater is held at a constant temperature of 100 ˚C. dQ/dk increases as the opening increases.

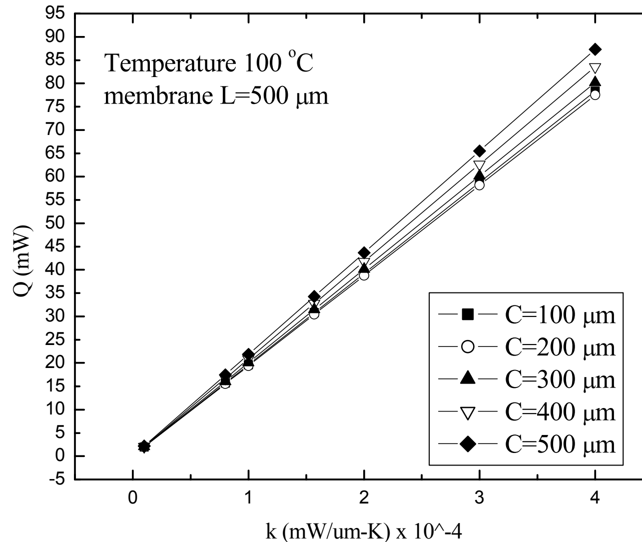

It is interesting to note that trapezoidal channel will give slightly better sensitivity than pyramidal channels for a given size. But the general trend still remains true, a larger C+L/2 leads to a greater sensitivity and a larger L for a given size yields a greater dQ/dk.

Fabrication

A miniature TCD can be fabricated using conventional silicon micromachining techniques. In summary the resistive heating elements are sputtered and patterned through the liftoff process. Afterwards silicon is anisotropically etched using potassium hydroxide (KOH) to define the channels and membranes.

Figure 13 depicts a cross sectional view (not to scale) of the starting material, a silicon (<100> orientation) wafer with low-pressure chemical vapor deposition (LPCVD) silicon nitride (Si_xN_y). The wafer is cleaned to remove contaminants and then goes through a series of photolithography steps. The photolithography steps are summarized below:

Solvent Clean (acetone/methanol/isopropanol)
Dehydration Bake
HMDS prime (photoresist adhesion promoter)
Spin on photoresist
Align mask, expose to UV light, develop, rinse in DI water
Inspection

The first mask finds the 110 plane. This is to ensure that the suspended membrane and channels will be formed correctly. The next mask defines the resistive heating elements, as seen in Figure 14. After the wafer is patterned, we sputter 200 Å of chromium followed by 5000 Å of platinum.   Materials, that are resistant to the potassium hydroxide etchant, must be utilized. Properties of the metals used can be seen in Table 1. After the metal deposition the wafer is placed in an acetone bath for several hours, in order to “lift” the *unwanted* metal. The sputtered platinum is then annealed in ambient nitrogen at 500 ^{o}C.   The annealing process reduces the stress of the platinum film.

Table 1. Properties of metals used. [CRC handbook]

Metal	Thermal expansion coeff. (10^{-6} K^{-1})	Electrical Resistivity (10^{-8} ohm m)	Bulk Density (g/cm^3)
Chromium	4.9	12.6	7.15
Platinum	8.8	10.7	21.5
Gold	14.2	2.26	19.3

After the platinum is annealed, we perform another series of photolithography steps to pattern the gold contacts for the wire bonds. The contacts are 1 micron thick with a 200 Å layer of Cr for adhesion. After the bond pads are made, the wafer etch openings are patterned; depicted through Figure 15. The nitride is etched using a CF_4/O_2 plasma. The nitride serves as a hard-mask for the KOH etching. Another possible hard-mask for KOH is silicon dioxide; however the selectivity is not as good, since it etches in KOH at a rate of 28Å/min. [Madou, 1997 p.171] Moreover, the LPCVD silicon nitride is a low stress robust material. A detailed process flow, deposition and etching recipes can be found in Appendix B.

Figure 13.   LPCVD silicon nitride wafer.   Because the nitride serves as a hard-mask for the KOH etch, it must be deposited on both sides of the wafer.

Figure 14. Silicon Nitride wafer with sputtered chromium adhesion layer (200 A) and platinum resistor (5000 A).

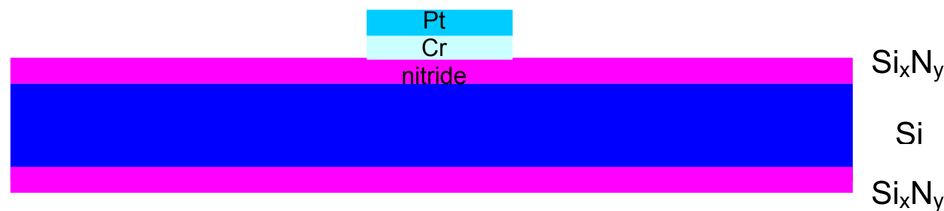

Figure 15. Patterned nitride, top (top) and cross sectional views (bottom). The nitride serves as a hard mask for the KOH etch.

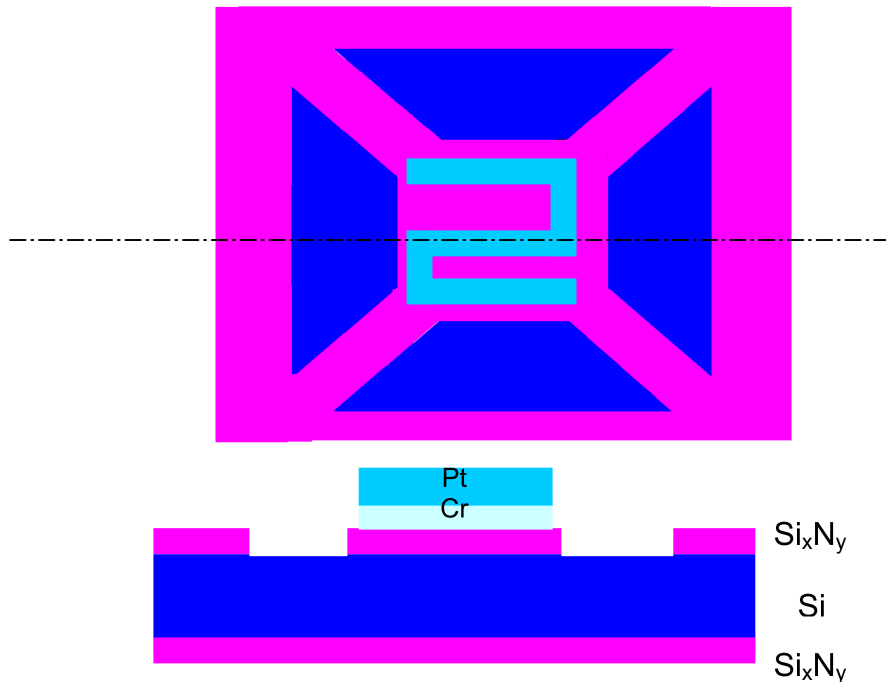

Once the nitride is etched, the photoresist is stripped and the wafer is cleaned. The wafer is placed in a KOH bath at 85 °C. At this temperature, silicon etches at a rate of 1.4-2.0 µm/min (in the <100> direction), with an etch rate ratio of 400 of the (100)/(111) planes and an etch rate ratio of 600 for the (110)/(111) planes. However, if the wafer is left in the KOH bath long enough the wafer will etch in the <111> direction, and undercut the nitride mask, forming the suspended membrane, as shown in Figure 16.

Figure 16. Anisotropically etched silicon wafer. Plane directions are shown. In this case, the wafer has been etched through.

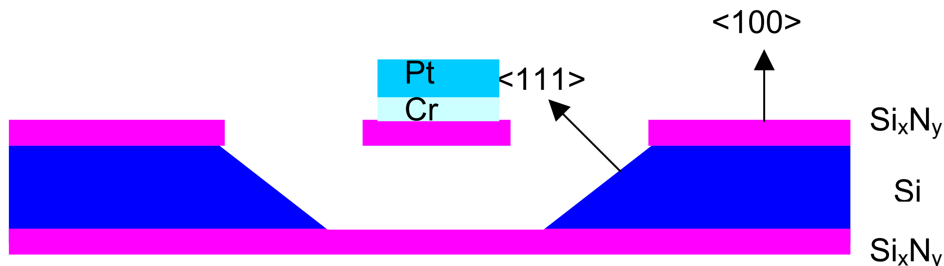

An SEM picture of a finished channel and membrane is shown in Figure 17. Figure 18 depicts a patterned resistor atop a nitride membrane. Figure 19 illustrates the gold bond pad. The sidewall of the gold bond pad is very rough, presenting one of the disadvantages of the liftoff technique. However, the resistors show very nice smooth sidewalls.

Figure 17. SEM image of micro-TCD cross-section. Suspended membrane remains standing after being diced in half showing its low stress.

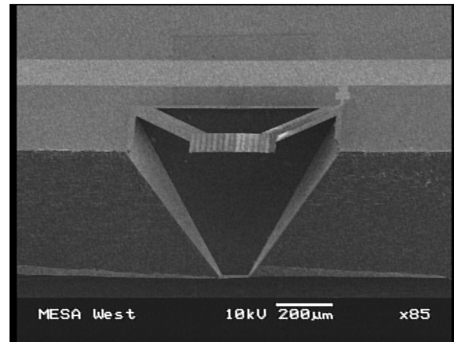

Figure 18. Deposited and patterned resistor on suspended silicon membrane.

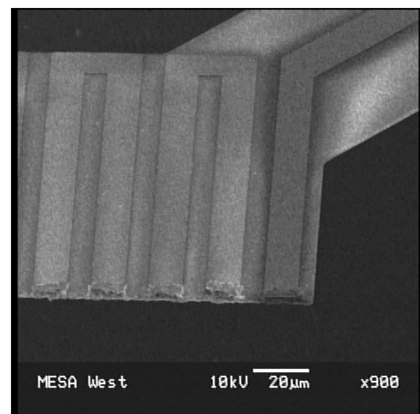

Figure 19. Deposited and patterned gold bond pad, 1 µm thick with 200 Å layer of chromium for adhesion

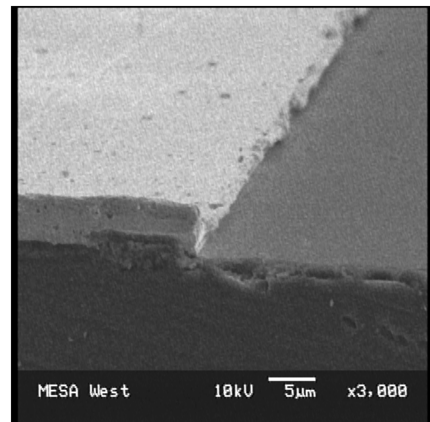

After the potassium hydroxide etch, the wafers are rinsed in DI water. Once the wafers are etched, they are rinsed until water resistivity (18 Ω) is reached. The wafers are then solvent cleaned and rinsed in DI water once again. They are then heated up to 90°C in a hot plate and crystal bond is applied to the wafer to hold the membranes together during the dicing process. After the wafers are crystal bonded, the individual die is

diced. The dies are then wire-bonded to a 24-dip pin package for simple electrical connections (Figure 20).

Figure 20 Wire-bonded part ready for fluidic connections (left) and completed part (right) ready for testing.

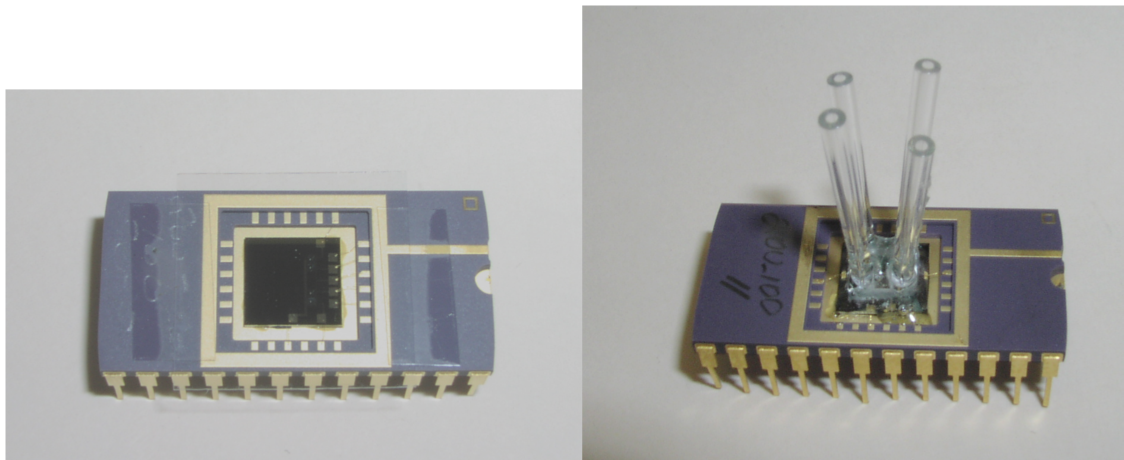

After the die is packaged lids are epoxied to the die to provide interfaces for fluidic connections. The lids are designed for either parallel flow or perpendicular flow and are pictured in Figure 21. Care must be taken to create a gas tight connection between the lids and the die substrate without breaking any of the wire bonds. Typically a UV-cured cement is used to tack the lid to the surface. Capillary unions (double ended quartz capillary couplers of decreasing diameter coated on the interior surface with polyimmide) are cut in half and tacked to the lid to provide a fluidic tubing connection point. The entire die and lid are then encapsulated in 5-minute epoxy to create a gas tight seal. All devices are leak checked under pressure by submersion in water. Flexible Teflon tubing is inserted into this union to operate the device under helium flow.

Figure 21. Pyrex Lids and how they fit over device to accomplish perpendicular flow and parallel flow. There are two sizes to fit over the different sized TCDs. Restricting the flow path as narrowly as possible increases the sensitivity of the TCD in the perpendicular flow scheme.

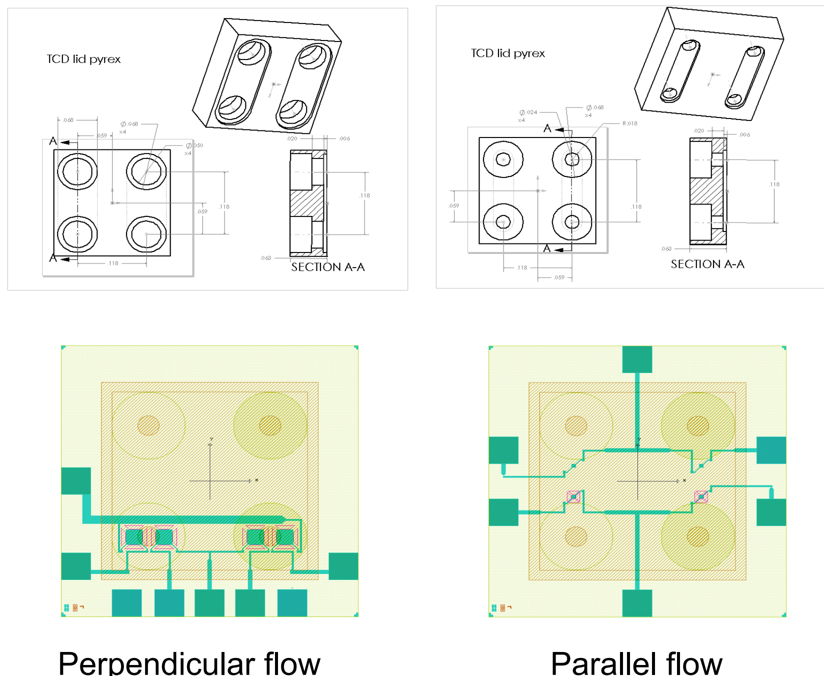

Bench Scale Experimental Results

There are three different die styles for the TCD related to flow and physical lay out on the substrate: parallel, perpendicular and dual. The parallel and perpendicular flow paths are illustrated in Figure 5. In each case the parallel style only has one suspended membrane per channel and a bridge resistor patterned on the surface as seen in Figure 21 B whereas the perpendicular style has two membranes per channel with one resistor on each membrane (Figure 21 A). The dual style was not developed through modeling but added as a design change on the mask as an empirical test. It is similar to the perpendicular device in that the flow impinged directly on the membrane. However, there is only one membrane per channel (reference and analyte) which supports both of the resistors in the Whetstone bridge (e.g. R1 and R3 are on the same membrane). This is likely to decrease the overall noise in the system but is not apt to increase the sensitivity. Nineteen unique designs were fabricated in parallel, perpendicular and dual styles. Differences are a function of membrane size, opening size and style. Each of the three styles had a unique wire out to the 24-pin package so each style needed its own breadboard for testing (Figure 22).

The packaged μTCD styles were then placed on an electric breadboard and connected to a power supply for individual testing.

Figure 22 Wiring diagrams for 24-pin DIP pin out for Parallel, Perpendicular and Dual TCD styles. Resistance varied from device to device so 1k was used as a placeholder. The starting resistance is not overly significant since this is a bridge circuit and as long as all resistances are equal the bridge will be balanced.

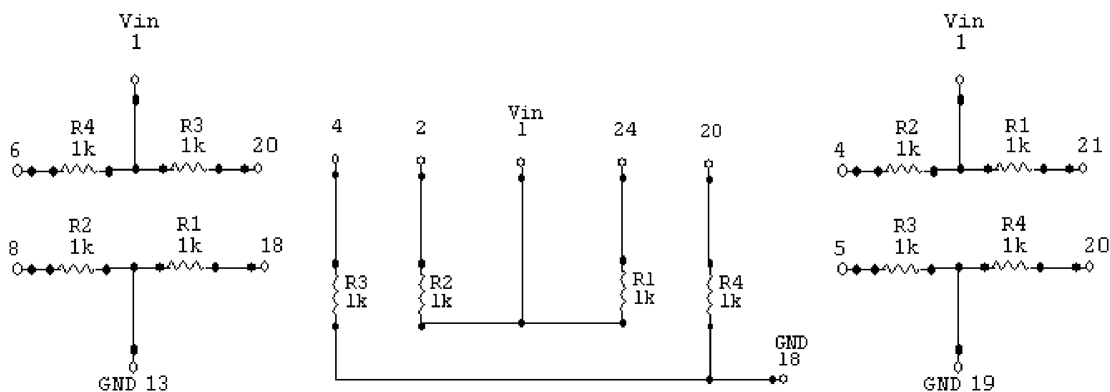

The µTCD was tested using helium as a carrier gas and air, toluene, carbon monoxide, nitrogen, benzene, toluene and xylene as analytes. Table 2 shows the thermal conductivity of the gases at various temperatures.

Table 2 Selected gases and their thermal conductivities at room temperature.

Gas	Thermal conductivity (mW/m-K)
H_2	183
He	157
CO	26
N_2	25
Toluene	14
Benzene	10

Figure 23 schematically depicts the test set up. Helium is supplied from a gas cylinder regulated at 20 psi. The flow is constricted with a needle valve and matched through both outlets (reference and effluent) via two more needle valves. Flow rates were checked using a bubble meter. A Swagelok™ tee was attached to each of the outflow from the needle valves. One side (reference gas side) was capped and the other side (sample detection side) was fitted with a GC septum and held in place with a Swagelok™ nut. This permitted the measured introduction of analytes using a GC syringe. All analytes were manually injected with a syringe. Toluene and benzene were injected as a mixture with air by pulling headspace gas samples from a vial containing liquid.

Figure 23. Experimental test set up for detector testing.

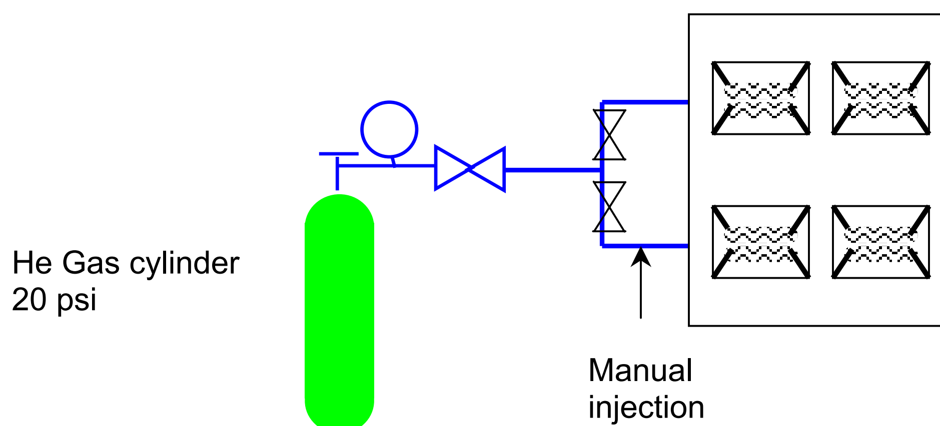

The TCD was wired in a Wheatstone bridge configuration and devices tested were four cell detectors as in Figure 1 B. Output readings were taken with an Agilent 34970A data acquisition system connected to a Dell laptop running Agilent's Benchtop software. The helium was supplied at a constant rate and then the voltage was applied to the device (to forestall oxidation of the filaments in air). Flow rates were varied, at 5, 10, and 15 sccm to assess the best operating conditions. A steady baseline reading is achieved and then the analyte is manually injected using a syringe.

Typical results are shown in Figure 24. The peak width at the FWHM is 5 sec. We integrated the peak areas to take into account any variability in the tailing. Tailing effects, as seen in Figure 25, are possibly due to varying flow rates from the gas. An analysis train is not present to fluidically dampen injection pressure differentials so that when the analyte is manually injected, a slight change in the flow rate is created. This change carries the analyte in a sweep rather than a pulse, thus creating the tail.

Figure 24. Time response of TCD for different concentrations of air (left). The carrier gas is He at 5sccm, the TCD is a membrane of 500µm with an etch opening of 100µm. The voltage is 5V (100 °C). Detector linear response. The peaks were integrated to assess the response. (right)

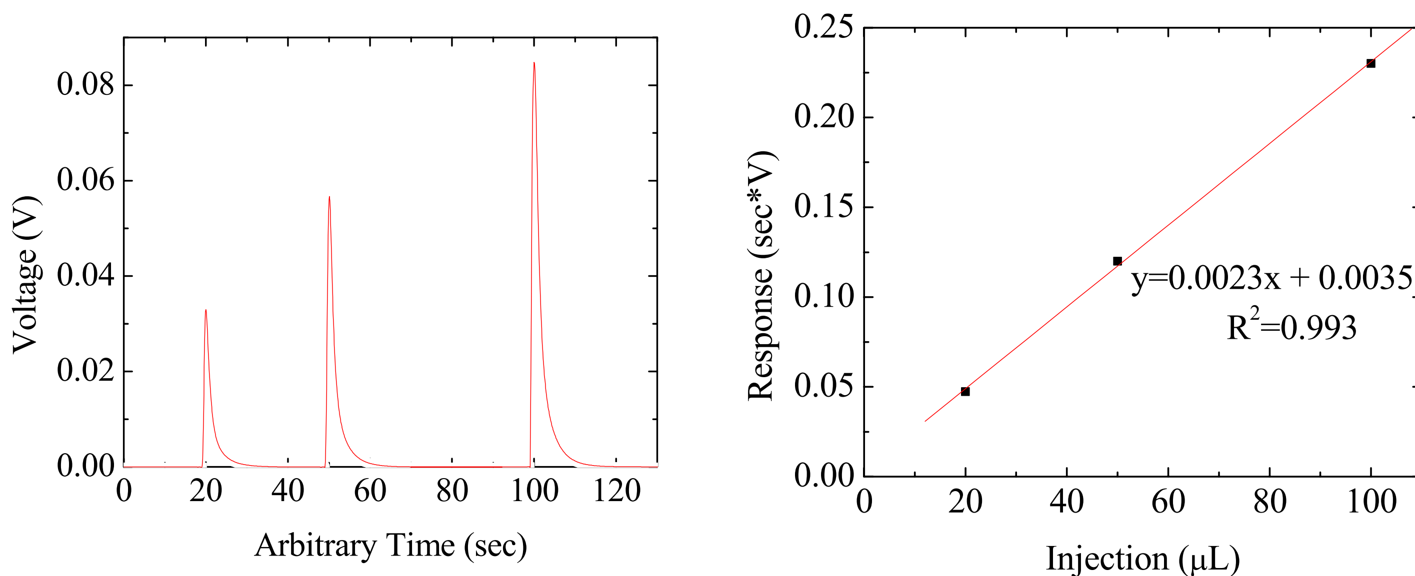

Air injections were made to assess the detector sensing capability and sensitivity of the different geometries. Manual injections of 100, 50 and 30 µL of air were made. All geometries show a linear response to varying concentrations of air. Figure 26 B illustrates the response for air and mixtures of toluene in air. The temperature of the heater was calculated using equation (1) and the temperature coefficient of resistance was determined by measuring the current at various voltages.

Figure 25. Time response for TCD for various concentrations of air. Detector used has a membrane size of 300 µm and an etch opening of 100 µm. He is used as the carrier gas and flowed at 5 sccm. (A) Close up of first peak tail from 30 seconds to 38 seconds. The tail is shallow and has a sharp drop (B). Close up of third peak's tail from 100 seconds to 140 seconds. (C)

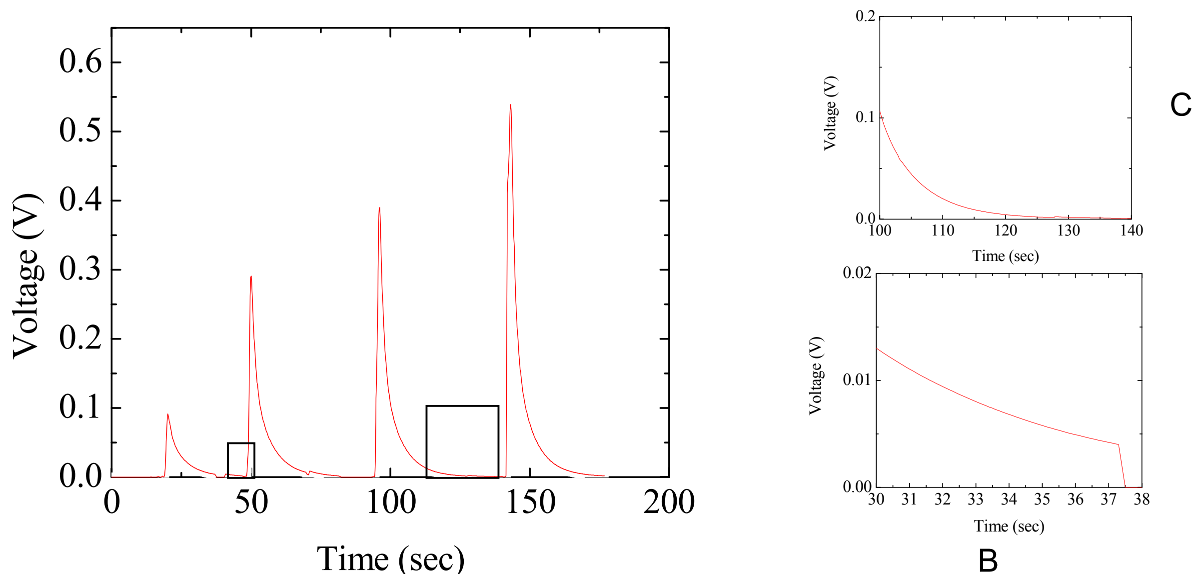

Figure 26. Time response for toluene/air mixture. Device is configured in perpendicular flow and dimensions are L=300 µm, C=100 µm, temperature is 300 ^{o}C. (A). Linear response of device to air and toluene/air mixture at various concentrations (B).

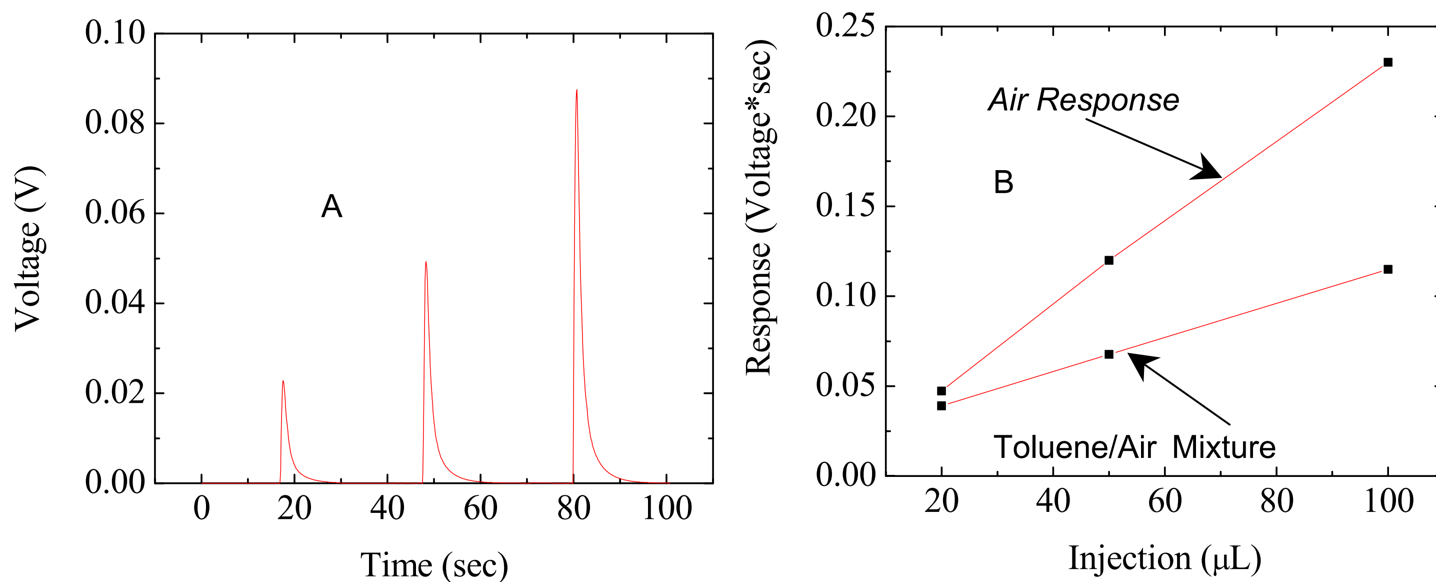

A mixture of toluene and air was also tested to ensure that the response peak would differ (the mixture will have a different thermal conductivity). The response for the same test conditions for a mixture of toluene in air is seen in Figure 26 A. The linear response can be seen in Figure 26 B. As shown, the response is lower than that of just air. Indicating that the detector is responding to the gas change in thermal conductivity.

The results are in good agreement with the simulation, as shown in Figure 27. It confirms the general trend that higher temperature will yield higher sensitivity. The results also show that larger geometries at higher temperatures show higher sensitivity. This is in good agreement with the simulation indicating that ignoring the convection component of the thermal transfer in the modeling was at least a good first approximation.

Figure 27. Experimental results and simulation. The device is a membrane with length of 500 μm and an etch opening of 100 μm. However, both resistors are suspended on the membrane (dual configuration).

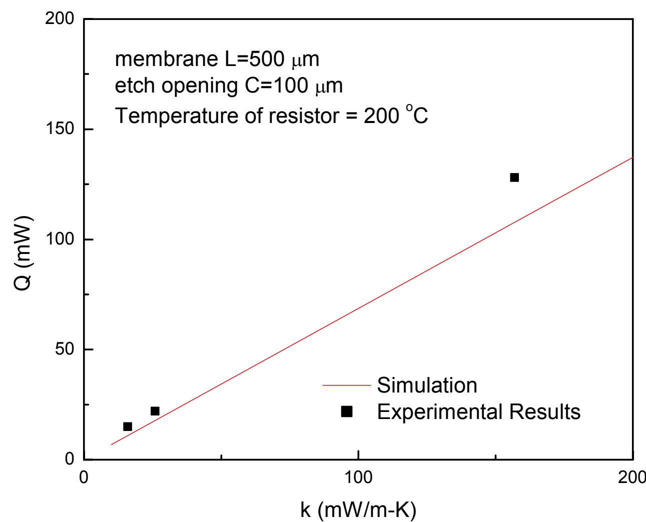

A design of experiment (DOE) was performed to assess the effects of all factors: geometry, flow type, voltage, and flow rate. The DOE matrix is presented in Table 3. We tested two styles (parallel and perpendicular flow), three voltages (6,8,10) and 3 flow rates (5, 10 and 15 sccm). The general results were that within the parameters that were selected indicated that larger geometry with higher voltages and lower flow rates had the highest sensitivity. The perpendicular design was the most sensitive followed by the parallel design. The dual design was the least sensitive of the three.

Table 3. Design of Experiment Matrix.

Geometry	Flow Type	Voltage	Flow Rate
200_100	Parallel	8V	15 sccm
200_100	Perpendicular	10V	10 sccm
300-100	Perpendicular	8V	5 sccm
300-100	Parallel	10V	15 sccm
200_100	Parallel	6V	10 sccm
300-100	Parallel	10V	5 sccm
200_100	Parallel	6V	5 sccm
300-100	Parallel	8V	10 sccm
300-100	Perpendicular	6V	10 sccm
200_100	Perpendicular	8V	5 sccm
300-100	Perpendicular	6V	15 sccm
200_100	Perpendicular	10V	15 sccm

System Integration

Background

The TCD detector and complete analysis system was originally proposed as a design for process control within an industrial refinery setting. This required the detection of carbon monoxide, carbon dioxide and 2 carbon hydrocarbons (ethane, ethylene, acetylene) some at sub ppm levels. It was subsequently decided that the TCD detector was not likely to be of sufficient sensitivity for the intended application. A new design was proposed by the industrial partners using a commercial photo discharge ionization detector having lower detection limits than the projected limits of the TCD. Also the design and fabrication of a microvalve at Sandia was proposed for a high-pressure sample collection and injection into the system. The TCD system development was continued as a back up in case the new design encountered problems and to have a system ready for other industrial customers for possible collaboration. Since it was assumed that the original analyte set (primarily gas phase under ambient conditions) could not be detected adequately with this system a new set of analytes needed to be chosen to test the system. A standard analyte set used to test the resolving power and sensitivity of a chromatographic system is benzene, toluene and xylene (BTX). These were used because they were easy to capture on preconcentrators, liquids under ambient conditions with reasonable vapor pressures, detectable with the TCD and could be used to qualitatively measure the resolving power of the GC column used for separation.

Sandia has developed a handheld gas-phase µChemLab for the detection of chemical weapon agents. This system is composed of three microfabricated components: the preconcentrator (PC), column and SAW detector. The preconcentrator is a heating

filament suspended on a thin silicon nitride membrane for thermal isolation, see Figure 28. This membrane is coated with an adsorptive material to capture the target analyte. The adsorption layer is loaded with analyte over time then quickly release in a short pulse by fast heating of the membrane. This acts as the injection event into the system. By collecting sample over longer time periods, small amounts can be concentrated thereby increasing the amount of material sent to the analysis train. The preconcentrator can also act as a discriminator through the choice of coatings.

The column is a high aspect ratio (in cross section) spiral, reactively ion etched out of silicon (Bosch process). The columns are typically 86 cm in length and are capped with an anodically bonded Pyrex lid with two connection ports for introduction and outflow of carrier gas (Figure 28). The sidewalls of the column are coated with commercial liquid phase chromatographic coatings.

Figure 28 Microfabricated GC column (left) and preconcentrator. Nickel is included for size comparison.

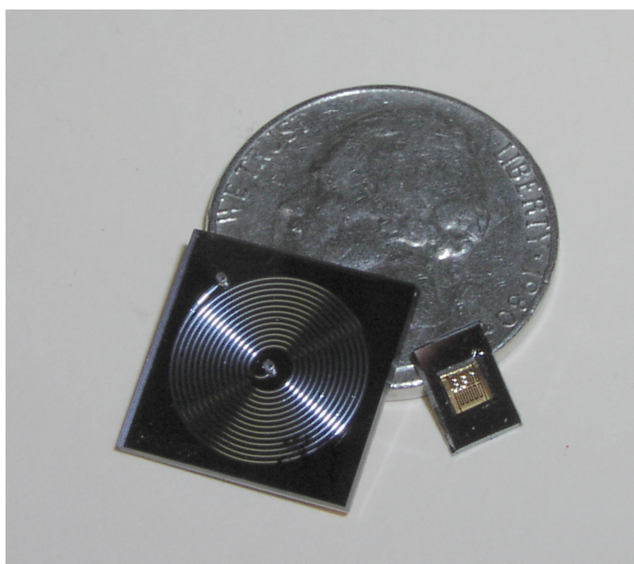

The SAW detector is an air stable detection system that can be tuned to have very sensitivity to specific semi-volatile compounds. The current detector is composed of a piezoelectric substrate with 3 application specific integrated circuits (ASICs) associated with it to it create and detect a ~500 MHz signal. The substrate is electrically excited to produce an acoustic wave on the surface of the material. Pickup lines some distance form the launch lines convert the acoustic signal back into an electrical signal. By adjusting the chemical composition (through the use of surface deposited polymers) of the area between the launch and pickup lines compounds can be made to interact with the surface. Mass differences change the phase of a launched wave in modified area versus a reference wave on a nearby uncoated active area. This is essentially a very sensitive mass detector. The TCD is an intrinsic property detector that is effected by relative concentration of material present.

The plan was to build on previous designs for the µChemLab with some of the restrictions lessened. The standard µChemLab handheld unit runs on batteries and

uses air as a carrier gas. Since this was to be an emplaced process controller AC power was used. All of the electronics are DC and the system could be run from a battery supply if needed. Helium or hydrogen need to be used as a carrier gas for the TCD detector. This requires a gas supply bottle and regulator to feed the system. Helium was chosen over hydrogen for safety reasons in lab testing, however if the system needs to operate without a bottled gas supply a hydrogen generator may be a possible design change for future systems. Another plan for this system was as a test bed for adaptations and improvements that, if successful, could be incorporated into other µChemLab systems.

System Design

Having a detector that responds in a predictable way to analytes, a system needed to be built around the detector. A schematic of how this system was envisioned is shown in Figure 29.

Figure 29 TCD System schematic drawing

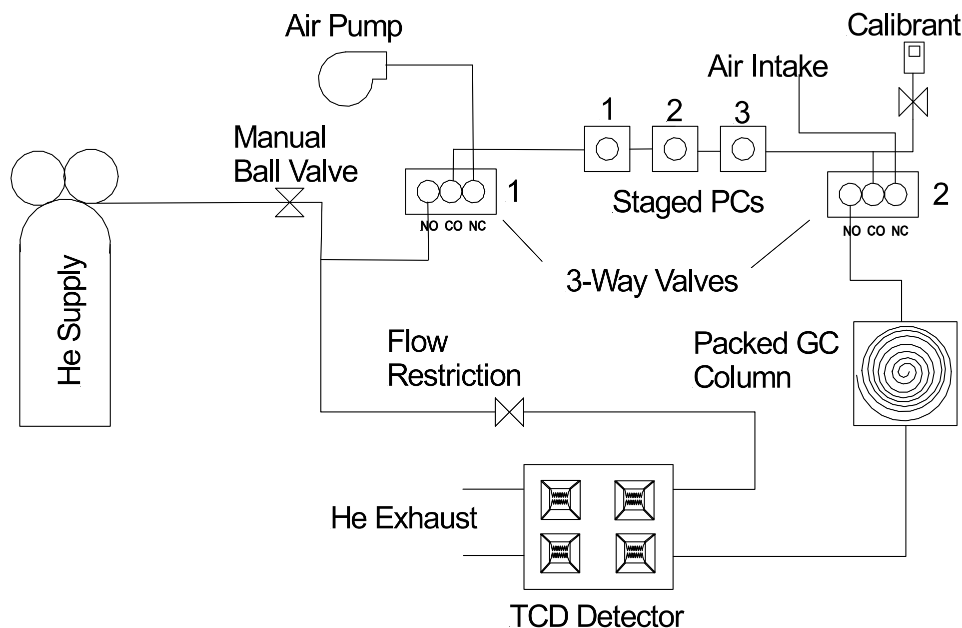

Helium is introduced from a regulator and is split into two channels, one goes through the analysis train and one goes directly to the reference side of the detector. Flow rates were balanced by using a restrictor on the reference side of the system. Following the analysis train helium flows through a 2-way valve into 3 separate PC holders. The gas then goes through another 2-way valve into the chromatographic column and into the analyte side of the TCD. Helium is then exhausted from the system from both the analyte and reference side of the TCD. The sample introduction is accomplished via actuation of the two mini-valves to an alternate flow (in this system it is open to air, however in practice it could be another pressurized flow system) created by a small diaphragm pump pulling gas through the 3 PCs and being fed from a bubbler through liquid analyte, assuring saturation of the PCs.

A typical run would start by supplying helium through the complete system to assure stead-state background conditions at the detector and bring the column to an isothermal temperature. This also makes sure that the detector and column are under an inert atmosphere while being heated. The valves are electrically switched and the pump is turned on to pull air and analyte through the PCs for a specified time period. The valves are then switched back and the system is purged for a few minutes to get rid of air and analyte vapor. At this point the system takes data for a few seconds to establish a baseline and the PCs are fired in a defined sequence and kept hot throughout the analysis once they have been fired. Data is typically taken for 2 minutes and the system can be reset and is ready for the next run. A calibration run would operate similar to the start of a typical run but instead of loading the analysis PCs and firing them off the valve to the calibration cell would be opened and the calibration PC would be heated to drive off the analyte.

Fluidic Interconnects Updates

Previous versions of the µChemLab have used permanent connections in the fluidic train, we wanted to employ a connection that could be made and broken many times without loss of integrity. Parts could then be swapped in and out of the system without excessive down time. These connections would preferably be screw fittings of small dimension that could create pressure tight seals between components and not require specialized tools to open and close. The solution was NanoPort fittings from UpChurch Scientific (Figure 30). This is a miniSwage-type fitting that can work with both small plastic (PEEK, Teflon, etc.) tubing or capillary tubing. These fittings are machined from polyether etherketone (PEEK) a high temperature chemically resistant nonporous polymer. A male fitting holds the tubing and a female adapter Swages the fitting down on the tubing as it is tightened. The fittings are tightened and released by hand. Tests with our system indicated that the NanoPort parts will maintain pressure tight connections up to 20 psi (ignoring permeation).

Figure 30 Commercial NanoPort fittings with Teflon tubing

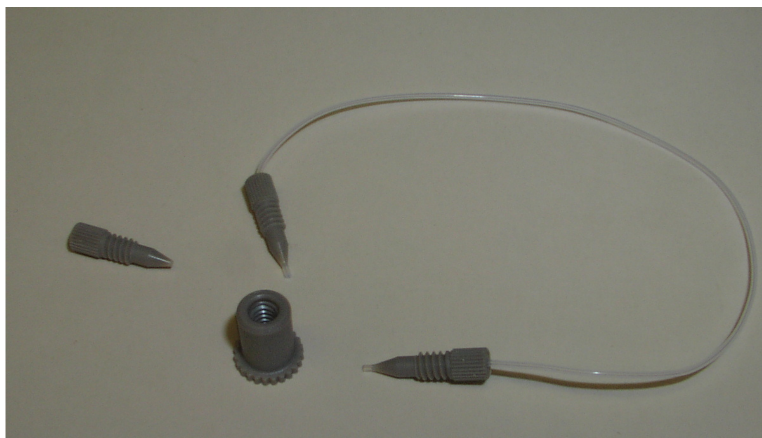

When working with semi-volatile compounds adsorption of material onto the walls of the tubing can effect the sensitivity and repeatability of the system. PEEK or chemically

deactivated quartz capillary tubing is typically used in the µChemLab. Since we were analyzing gases and/or volatile compounds, adsorption was not as much of a concern. Initial plans were to use large bore (530 um i.d) capillary columns as the tubing in the system. The bend radius of PEEK and capillary tubing prohibited fitting all of the components together in the footprint that had been selected. Therefore another type of tubing was needed. Helium has the undesirable property of permeating through any polymer due to its low molecular mass and high diffusion coefficient (69.7 mm^2/s). If we limited our system to only semi-volatile compounds (of limited diffusion coefficients), PTFE tubing was a suitable choice; it is nonreactive, available in the i.d. and o.d. needed and is very pliable so does not have the problems associated with bend radius. The system is unheated and remains at ambient temperatures except in the heated zones (GC column, TCD detector, and PCs). The PTFE was used only to interconnect components and was not used in any heated areas where higher temperatures could cause greater permeation rates.

Sampling System

The standard µChemLab system uses air as the carrier gas for the analysis train. This is achieved using a miniature diaphragm pump (Figure 32) pulling on the outlet of the system. Our TCD detector requires the use of a carrier gas such as He or H_2 in order to have reasonable sensitivity. Therefore the system has to operate under pressurization. Since this system was designed to be automated, a method for introducing samples needed to be designed. The preconcentrators can capture semivolatile analytes however they would need to be captured from an environment that is isolated form the analysis train. Therefore a system of mini-valves was created that allowed the loading of preconcentrators without the need to run air through the entire analysis train Figure 31.

Figure 31 Dual meso-valves used for sample introduction and analysis train isolation, mounted on backside of system box.

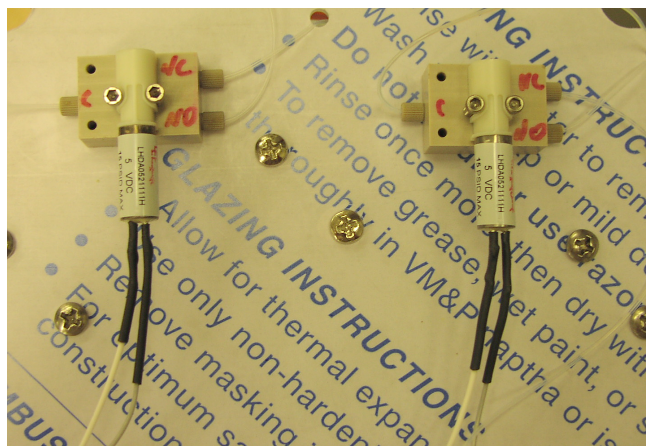

Figure 32 Miniature diaphragm pump used to load PCs

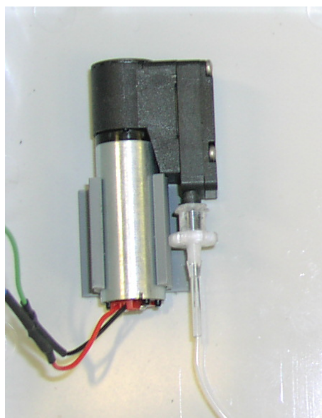

The detection limits required for the refinery application were lower than the expected capacity of our typical preconcentrators when compared with the reduced sensitivity of a typical TCD detector system. Therefore, multiple preconcentrators would need to be connected in serial between the sampling valves to allow the collection of greater amounts of material. It was also desirable to have a method of placing PCs in the system and be able to test them without destroying them removing them from the system. A holder was designed for the PCs that met this design requirement. Unfortunately sacrifices had to be made in terms of dead volume and an increase in the ”wetted” surface area. Using multiple PCs required the development of a timing circuit that would allow each preconcentrator to be fired serially to allow the release from each firing to be concentrated into a single pulse delivered to the system. The length of time that the PCs were fired, the time between firing and the relative start time for firing were all settable using the control program for the system board in the unit.

Figure 33 Design diagram of PC holder showing the lid and body with space for O-ring seal. The dark square in the center of the body is where the PC sits. Opening at base is for NanoPort™ connection that flows into square and out other side. This connects to another NanoPort™ on other side of part (hidden from view). Electrical contacts are made with the PC through the lid via pogo pins.

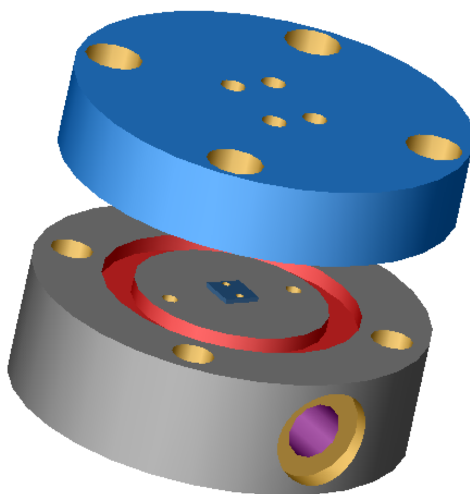

Novel Columns

The original application had the separation of gases as the required application; our standard open columns with commercial side-wall coatings are not able to resolve gases (just vaporized analytes). There are commercial solid phase column materials that can separate gases. Therefore a packable column was created with a square cross-section (300 μm X 300 μm), shorter length (20 to 29 cm) and posts positioned at the exit of the column to keep the packing material from entering the detector. Two different columns and packings were tested. One 20 cm column was packed with a commercially available prewashed 13X molecular sieve (100/120) material sieved down to 125 mesh (less than 125 um). A second column 29 cm long was packed with carbonaceous material produced through the controlled pyrolysis of polystyrene to generate beads of 75-150 um in diameter. These spherical beads were originally intended to be highly porous to allow gas separations but resulted in very low porosity (~3 m^2/gm). This material was also sieved down to 125 mesh. To allow the beads to participate in separations they were coated with polydimethylsiloxane (PDMS) a typical gas chromatographic column coating. Once the system was packed and tested as functioning properly it was prepared for incorporation in the system. This included the attachment of wire leads to the backside heater patterned onto the column, attachment of a thermistor on the front side of the column (along with associated leads) and the fluidic connections for the NanoPort fittings. The fittings were somewhat large for the columns we were using; therefore one of the fittings was milled down 65 thousandths on one side to allow them to sit side by side on the surface of the Pyrex column cover. These fittings were attached to the surface using 5-minute epoxy and then epoxied to one another for strain relief. Each column was tested for flow and leaks. The carbonaceous column is identified as OV1-50XP and required 9 psi of pressure for 2.8 ml/min of flow. The molecular sieve column is identified as 13X and required 20 psi to maintain 0.6 ml/min of flow. This system used an isothermally heated column for separations. In the typical μChemLab, the columns would be ramped to perform the best separation. Normally about 4-5 psi and 3 ml/min is required for the standard μChemLab system. The addition of these ports may hinder ramping rates due to the added mass and therefore higher thermal load during heating.

Figure 34 Completely assembled GC column packed with modified NanoPort female fittings and molecular sieve adsorbent. Wires on the right are thermistor leads; wires on the left are column heater leads.

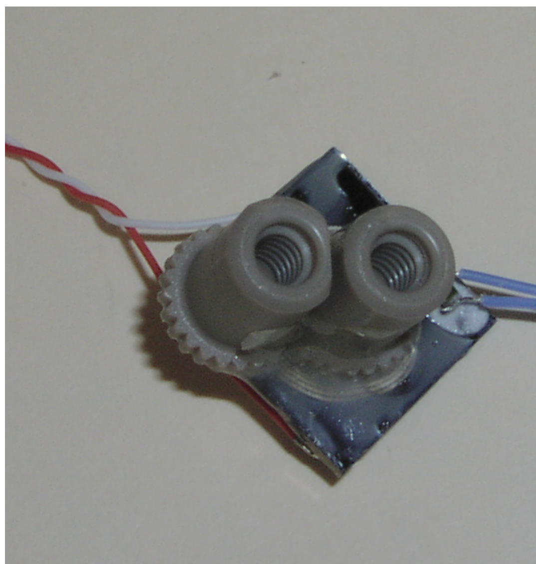

Detector Packaging

The lid arrangement used for bench testing the μTCD was not sufficient for incorporation into an automated system. A new lid was designed that fits into the original Pyrex lid Figure 35. This lid was then glued to the top surface of the 24-pin DIP to create a monolithic detection system that was thermally stable and modular. Two lids were fabricated from PEEK and aluminum. The aluminum lid was much easier to switch out due to its ability to withstand higher temperature without degrading. This facilitated the removal of an old lid by burning off the epoxy. A new detector can be placed in the system by merely removing the NanoPort fittings and popping the DIP out of the controller board.

Figure 35 Diagram of lid for TCD in transparent rendering to show NanoPort connections and face match with Pyrex lid.

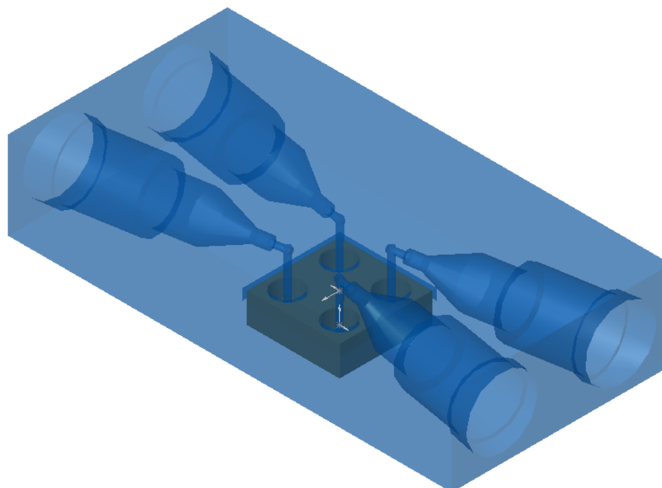

Electronic Controls

The system was controlled and output its data through an RS-232 port connected to a Windows computer running the standard µChemLab data collection program written in Microsoft Visual Basic 6.0. This VB program plots the data output in real time for all channels and then stores the data to an Excel importable format for further analysis. Parameters for each run were set via HyperTerminal and stored within the system until changed. The µGC electronics are based on the standard µChemLab board set but include a new sensor module, some additional controls, and different system control sequences. Most of these changes required that the firmware used to control the hardware be modified accordingly. The code controlling the system was written in C and allowed for a number of parameters within the system to be tweaked between runs including control of all heated components, heating rates, heating times, valve timing, pump draw timing and total run times. There are several major differences between a standard µChemLab system and this version of µGC. The differences are; PC loading, PC firing, analysis module hardware and control firmware. An important addition to the standard program was the ability to allow a rest time once the PCs were loaded with analyte. This was an opportunity to flush the system of air (captured during collections sequence) prior to PC firing and subsequent separation and detection.

Figure 36 Modified outlay of detector board to adapt the SAW detector electronics to the TCD system.

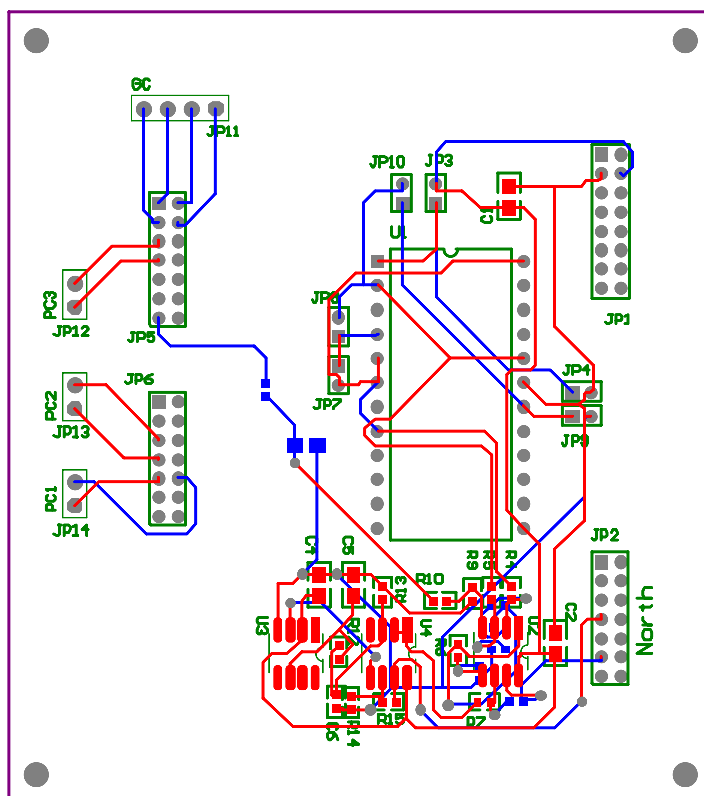

The µGC system required firing 1 to 3 PC's in sequence with programmable timing for each PC (total "on" time) and times between PC's. Since the µChemLab electronics board set includes two independent PC channels, two of the three could be easily configured in firmware. No electronics were available for the 3rd channel but since two programmable GC controllers were available (and only 1 would be used in this system) one of the GC controllers was reconfigured to function as a voltage controller for use with the 3rd PC. While this type of controller is not a temperature controller like the PC controllers (temperature is controlled via a resistance control loop circuit) it can be calibrated to give an approximate temperature by knowing the voltage vs resistance curve. Since the sensor in this system is not the usual SAW sensor, for which the standard electronics are designed, a voltage shifter was needed to adjust the sensor output levels for use with the standard µChemLab board set. An adaptor board was designed and fabricated, which included a difference amp, to take the difference voltage from the sensor bridge, to convert the ouput to a single ended output for the A/D converters. In order to match the A/D input range the output from the difference amp was run through a voltage shifter, which could shift the output into the 1-3 volt range of the A/D converter. A preferential direction was assumed for the bridge polarity when the buffer circuit was developed. This assumption turned out to be a problem since in the development circuits there was no preferred bridge polarity. There are several easy fixes for this problem, without addressing how to "tune" all the sensors to the same

polarity and response, but in the current layout the fixes were not implemented. The easiest method (with the existing hardware) is to use an extra A/D channel. In addition to the sensor package and electronics the adaptor board also provided I/O connectors for each of the PC's, the single GC, and a temperature sensor in the proximity of the sensor package. This allowed for verification that the data collection system was working since it could be manually cooled or heated during the system run and cause subsequent rise or fall in an otherwise constant output signal.

Completed System

The complete analysis system (minus carrier gas source, power supply, and pressure regulation see Figure 37) fit into a box 6 ¼" X 9 ½" X 5" in dimensions. The LCD display provides local feedback as the system goes through it's analysis routine. A suitable power supply could be easily incorporated into the system if AC line power is available. Complete output of data requires a computer, but it does not need to be collocated and the data is transmitted over a standard RS-232 interface.

Figure 37 Complete system. PCs are in the numbered cylinders on the right side of box, TCD is at the center, the column is suspended to the lower right and LCD output display is at lower left.

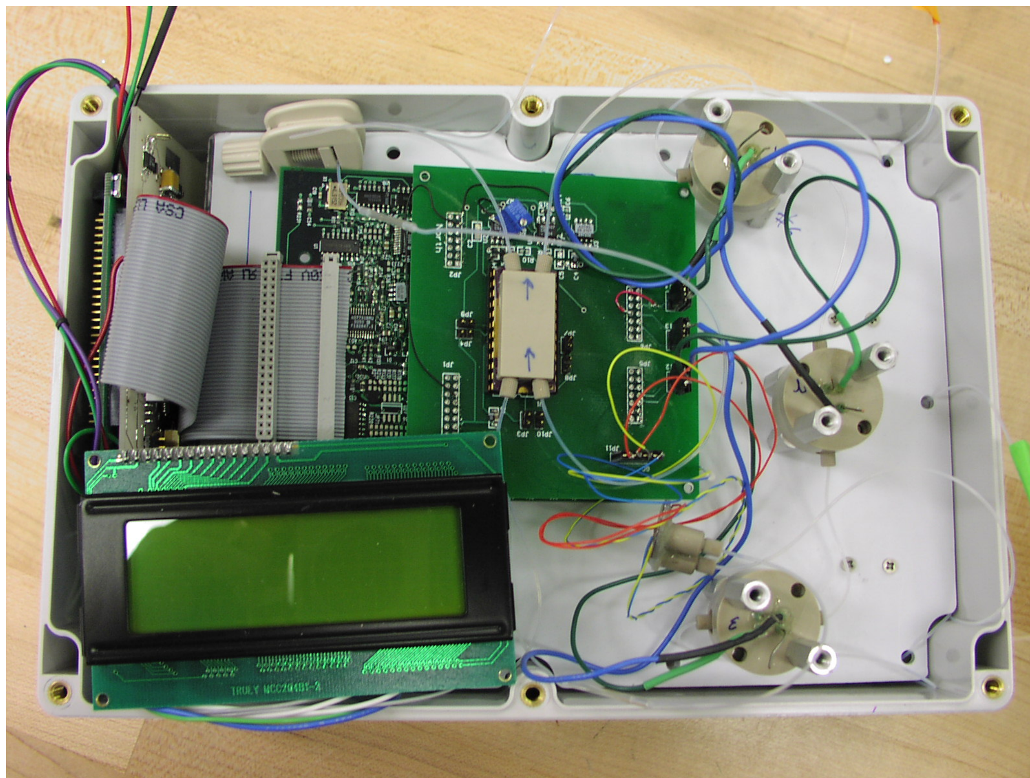

Discussion
The simulation results indicate that a larger geometry is optimum for the TCD detector; however this requires more power and voltage to achieve the same temperature as in a smaller device. Therefore the obvious trend is that a smaller device has better sensitivity if it can be maintained at a higher temperature than the surrounding materials without effectively raising their temperatures. The microfabrication of the TCD is straightforward and yields devices that are functional. The TCD is able to detect 100 ppm levels of CO in He and ppb level detection looks very promising based on a calculated signal to noise ratio of 10,000.

Figure 38. Time response of μTCD for 100-ppm CO in He. Device is configured in perpendicular flow; dimensions are membrane 500 μm and etch opening of 100 μm. This is data from the bench scale testing, not the system test. He is used as the carrier gas and flow is 5sccm.

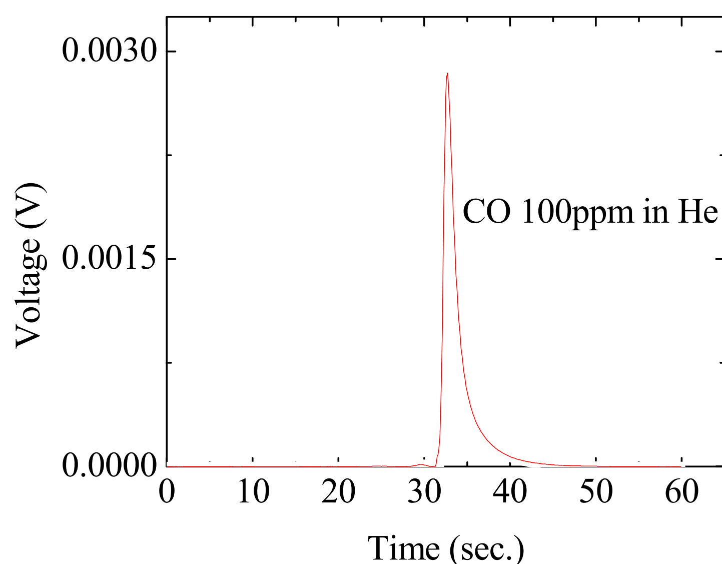

Verification that the detector is a concentration detector and not a simple mass detector was verified by injecting 50 μL and 100 μL of 100 ppm CO in He. This resulted in peaks of very similar area and response factor.

The NanoPort fittings seemed to work well with no obvious (submersion bubble checks) leaks during dozens of make/break connections adding and removing components from the system. Future use would need to explore a more rigid and less gas permeable material to allow for quantitative measurements. The female connectors into the PC fixtures and the TCD lid also worked well. The PC fixtures were especially useful in swapping in and out components without having to disassemble and reassemble the entire system (current μChemLab design). The bidirectional sampling system worked well for collecting material onto the PCs however there was some problem removing material at different PC locations (see below). However the programmed valve switching and negative pressure air collection system loading worked as expected.

Data output from the system resulted in 6 (x,y) pairs of voltage ticks vs. time in milliseconds. This is from the dual channel SAW system of the normal gas-phase µChemLab where each SAW has 3 output channels. These (x,y) pairs are designated A-F. Two of the A-D converters were tied to the TCD output to generate a dual output signal with different timing (channels B and D) and another of the outputs was tied to an onboard thermistor (channel E). The baseline drift inherent in the system is obvious in Figure 39. This could be from thermal effects, flow effects or air bleed through the system following collection. Attempts to allow the system to purge with helium prior to analysis did not seem to affect the baseline.

Figure 39 Data from system showing two output channels used for collection. The signal is inverted because the bridge and reference had to be switched to allow the differential output across the bridge to remain within the range of the A-D converters. Channel B and D output, which is overlaid illustrating firing of a single preconcentrator loaded with benzene, toluene and xylene.

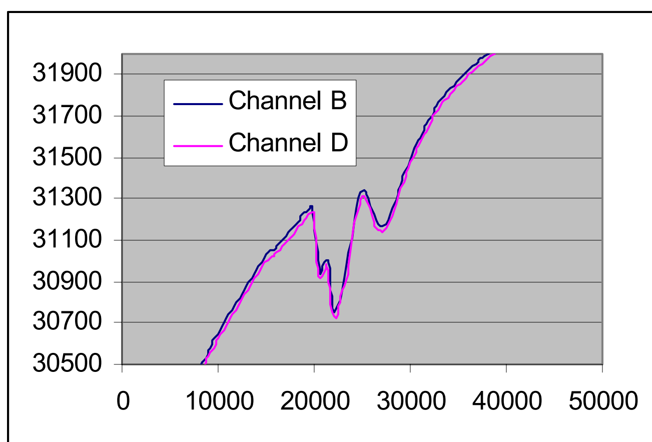

The offset differential between the signals of channels B and D was related to the baseline offset of each A-D converter. The other three channels returned timing info but null-data output (channels A, C and F). In each case the first A-D output (Channel B) was used in analysis for consistency. Pictured below is a typical data output stream from the thermistor, which is unshielded and some distance away from the detector. The TCD will show sensitivities to changes in flow, temperature and backpressure.

Figure 40 Thermistor output data from system during typical run. Notice that the variance is about 80 ticks whereas for the data in above figure has a differential of near 400 ticks, peak to baseline.

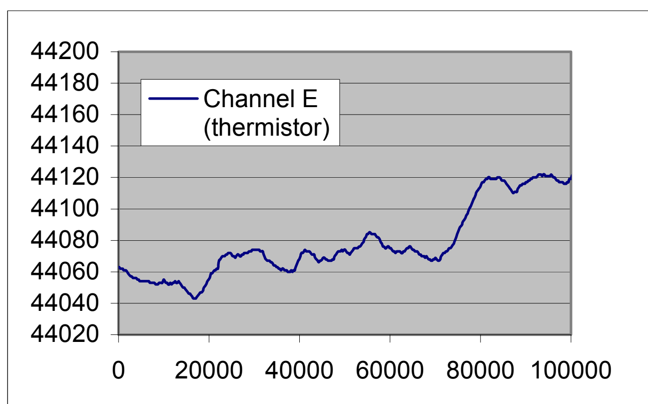

Numerous trials were attempted to overlap output from the multiple PCs however this was never satisfactorily achieved in this system. This may be due to inconsistencies in the fabrication of PCs and the relatively high detection limits of a TCD versus other detectors. Output using toluene as the captured analyte and three PCs is illustrated in the following figure.

Figure 41 Data channels B and D again. This is toluene fired off three preconcentrators. Two PC pulses appear to have combined with a third PC pulse lagging.

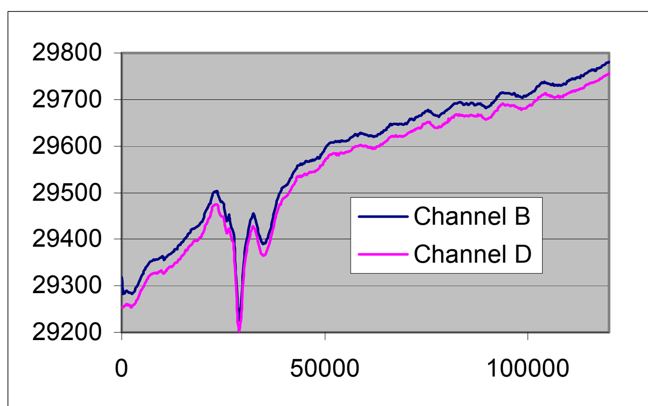

One PC consistently fired and released a large pulse of analytes. Perhaps the PCs are inconsistent but moving the PCs from fixture to fixture did not seem to help the problem. Therefore it may be a timing or pulse width problem with the controller software, available time did not allow us to determine the cause of this abnormality and it will be addressed in future systems. A single PC was therefore used for the multiple analyte system testing trials to simplify the data interpretation.

Three different columns were attempted with the system. The two packed columns mentioned in the System Integration section (OV1-50XP 28 cm and X13 20 cm column) as well as an 86 cm long high aspect ratio OV-1 (similar to PDMS coating) gas column. Each of these columns was tested on a full size GC-FID system for performance.

Baseline separation of BTX was achieved on the OV1-50XP column at 40 °C, 9 psi head pressure and 2.8 ml/min flow rate. Baseline separation of methane. ethane, ethylene and acetylene was achieved on the 13X column at 120 °C with a head pressure of 20 psi to get a flow rate of 0.6 ml/min. The standard OV-1 column was able to separate BTX at 40 °C as well. The 13X column had trouble allowing sufficient flow for the TCD detector (seems to need greater than 3-4 ml/min). This was most likely due to high backpressure from the small particles used for packing the column (sieved below a specific diameter but a large amount of dust below the sieved size was evident). The required pressure on the standard OV-1 column was somewhat lower due to its relaxed restriction (100 um X 400 um cross section and 86 cm long) vs. a packed bed. A comparison between the normal high aspect ratio column and the packed coated column indicates that the packed column is a better configuration for the test analytes used at flow rates and mass loadings needed for the TCD system. Moderate separation was achieved with the OV1-50XP column whereas almost no separation was observed using the standard high aspect ratio column at a similar flow rate within this system. This is surprising given the relatively similar separation of BTX by each of these columns on the full size GC-FID system. Calculations indicate that a 28 cm long packed and coated column using 125 um diameter beads will have a similar available surface area (neglecting sphere to sphere interaction) as the high aspect ratio column at 86 cm. Therefore it is unknown why the standard column performed so poorly with respect to the packed column. The standard column was one that is known to separate semi-volatile compounds relatively well. It did not have NanoPort connections and this may have contributed to its lower performance. Further work needs to be performed to compare the packed column against other known columns and analyte sets to fully understand this result.

Conclusions

We have designed, simulated, fabricated and tested a microfabricated thermal conductivity detector. The boundary element algorithm for the simulation demonstrates that rapid computational prototyping is advantageous and a great resource in the design of micromachines. Boundary element algorithms are efficient since only the surface, not the whole volume, needs to be discretized. We show that the simulations accurately predicted the tests results. Fabrication of the device is simple, although not trivial and ensures good precision and uniformity between devices.

A system has been developed and fabricated to demonstrate the capture separation and detection of analytes using a TCD detector. This system has not been optimized, this will have to wait on development for a specific industrial application however a number of elements have been incorporated and demonstrated within this system to allow application and innovation to other total microanalytical systems based on gas phase detection. The point was not to create a prototype system that could be deployed but rather to use the system as a test-bed of a number of new and innovative design changes that have the ultimate result of increasing the utility of the μChemLab analytical platform. Figure 42 shows qualitatively the detection of benzene, toluene and xylene being eluted from a micro-GC. The mixture was prepared using a planar pre-concentrator at 500 ºC with helium used as the carrier gas. The signal has been

inverted and the baseline adjusted to illustrate better the peak separation and relative size.

Figure 42. Detection of benzene, toluene and xylene eluted from µGC. TCD detector is membrane 300 µm and etch opening of 100 µm.

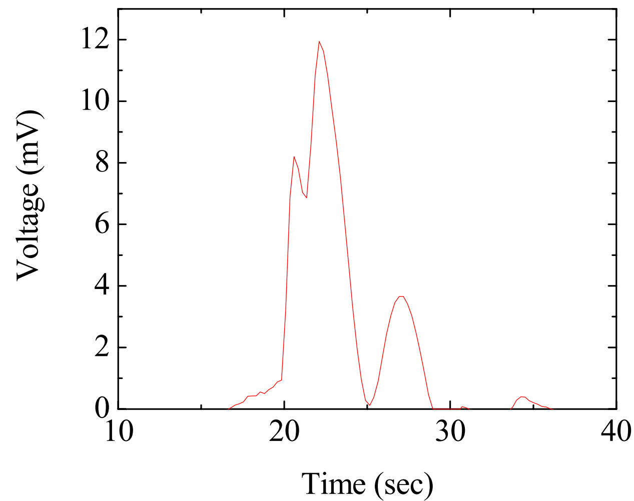

The test result indicates that the µTCD is able to detect gases at 100-ppm level concentrations and shows promise for testing sub-ppm levels. This is ultimately dependent on the thermal conductivity of the target analyte and is not generally applicable to all gases.

Definitions

a	horizontal distance from edge of bottom opening to upper edge of sidewall (m)
c	distance from edge of heater to upper edge of sidewall (m)
Cp	heat capacity at constant pressure (W/kg/K)
D	wafer thickness (m)
k	thermal conductivity (W/K/m)
L	width of square of heater (m)
Pe	Peclet number (convective heat transfer/conductive heat transfer)
Q	heat flow (W)
$\vec{q}$	heat flux (W/m^2)
R_f^o	electrical resistivity (Ω-m)
W_t	width of entire cell (m)
W_b	width of bottom opening of channel (m)
α	thermal diffusivity (m^2/s)
α_t	temperature coefficient of resistance (per degree C)
ε	radial emissivity (dimensionless)
ρ	density (kg/m^3)

Stefan-Boltzman constant. (5.67051×10^{-8} $W/m^2/K^4$)

Appendix A: Boundary Element Formulation and Solution of Laplace's Equation

Laplace's equation governs the steady state temperature T, and is given by

$$\nabla \bullet \nabla T(\vec{r}) = 0, \qquad \vec{r} \in V \qquad \text{(A.1)}$$

where $\vec{r}$ is the position vector in the region given by V, and ∇ is the gradient operator. The heat flux $\vec{q} = -k\nabla T$, and/or the temperature are generally specified on the surface S that encloses V. The thermal conductivity k, is assumed to be known and constant. For a unique solution, the temperature must be specified on at least one part of this enclosing surface.

The Green's function for Laplace's Equation satisfies

$$\nabla' \bullet \nabla' G(|\vec{r} - \vec{r}'|) = -\delta(\vec{r} - \vec{r}') \qquad \text{(A.2)}$$

where $\delta(\vec{r} - \vec{r}')$ is the Dirac Delta function and ∇' is the gradient operator with respect to the primed coordinate $\vec{r}'$. The Dirac Delta function is defined such that

$$\int_V \delta(\vec{r} - \vec{r}') f(\vec{r}')\, dV' = f(\vec{r}) \qquad \text{(A.3)}$$

where $f(\vec{r})$ is an arbitrary function of $\vec{r}$. The free space Green's functions in two and three dimensions that satisfy Eq. (A.2) are given in Table A.1.

Table A.1. Green's function and normal component of the gradient of the Green's function for Laplace's Equation♣ [Arfken, 1985, p. 912].

Dimensionality	$G(R)$	$\nabla' G(R) \bullet \vec{n}'$
Two	$-\frac{\ln(R)}{2\pi}$	$\frac{[n_{x'}(x - x') + n_{y'}(y - y') + n_{z'}(z - z')]}{2\pi R}$
Three	$\frac{1}{4\pi R}$	$\frac{[n_{x'}(x - x') + n_{y'}(y - y') + n_{z'}(z - z')]}{4\pi R^3}$

♣$R \equiv |\vec{r} - \vec{r}'|$, $n_{x'}$, $n_{y'}$, and $n_{z'}$ are the Cartesian outer normal components.

The boundary integral form of Eq. (A.1) can be obtained by multiplying Eq. (A.1) by the Green's functions G, and integrating over the region to obtain

$$\int_V \left[G\left(\left|\vec{r}-\vec{r}'\right|\right)\nabla' \bullet \nabla' T(\vec{r}')\right] \quad dV' = 0 \tag{A.4}$$

By using Green's Theorem [Arfken, p. 58, 1985], Eq. (A.4) reduces to

$$0 = \int_V T(\vec{r}')\left[\nabla' \bullet \nabla' G\left(\left|\vec{r}-\vec{r}'\right|\right)\right] dV'$$
$$+ \int_S \left[G\left(\left|\vec{r}-\vec{r}'\right|\right)\nabla' T(\vec{r}') - T(\vec{r}')\nabla' G\left(\left|\vec{r}-\vec{r}'\right|\right)\right] \bullet \vec{n}' \, dS' \tag{A.5}$$

The outer normal and bounding surface of region V are given by $\vec{n}'$ and S, respectively. Substituting Eq. (A.2) into Eq. (A.5), and using Eq. (A.3) results in the boundary integral form of Eq. (A.1)

$$\eta(\vec{r})T(\vec{r}) = \int_S \left[G\left(\left|\vec{r}-\vec{r}'\right|\right)\nabla' T(\vec{r}') - T(\vec{r}')\nabla' G\left(\left|\vec{r}-\vec{r}'\right|\right)\right] \bullet \vec{n}' \, dS' . \tag{A.6}$$

The integration in Eq. (A.6) is over the primed coordinates. The function $\eta(\vec{r})$ is 1, ½, or 0 when $\vec{r}$ is located inside the region, on the boundary, or outside the region, respectively [Brebbia and Dominguez, 1992, p. 50; Kane, 1993, p. 37]. Notice that for $\vec{r}$ on the boundary, Eq. (A.6) is in terms of only the conditions at the boundary, without any information interior to the region. This greatly simplifies the analysis because the unknown heat flux or temperature at the boundary can be determined without solving for any temperature interior to the region. In addition, as will now be shown, only the boundary needs to be discretized with a mesh of elements, which is far easier that discretizing the entire region as would be required for finite element or finite difference methods.

In this work, Eq. (A.6) for three-dimensional regions is discretized with constant elements, consisting of triangular or quadrilateral planes as shown in Figure A.1. Thus $\nabla' T(\vec{r}') \bullet \vec{n}'$ and $T(\vec{r}')$ are taken as constants on each element. The nodal point of element i is located at the geometric center of the element, and is given by $\vec{r}_i$ [Gelbard and Malloy, 2001].

With this discretization, Eq. (A.6) reduces to the boundary element form of Laplace's Equation, which is

$$\frac{T_i}{2} + \sum_{j=1}^{N} T_j \int_{\substack{S_j \\ j \neq i}} \nabla' G\left(\left|\vec{r}_i - \vec{r}'\right|\right) \bullet \vec{n}'\, dS' = \sum_{j=1}^{N} \left(\nabla' T(\vec{r}') \bullet \vec{n}'\right)_j \int_{S_j} G\left(\left|\vec{r}_i - \vec{r}'\right|\right) dS' \qquad \text{(A.7)}$$

(i = 1, ..., N)

where S_i, T_i and $\left(\nabla' T(\vec{r}') \bullet \vec{n}'\right)_i$ are the boundary, temperature, and normal component of the temperature gradient, respectively, of boundary element i. The total number of boundary elements is N. For each element either T_i or $\left(\nabla' T(\vec{r}') \bullet \vec{n}'\right)_i$ are specified as a boundary condition on Eq. (A.1). Therefore, either $\left(\nabla' T(\vec{r}') \bullet \vec{n}'\right)_i$ or T_i, respectively are unknown on all the elements. This set of N unknowns is determined by solving the N linear algebraic equations given in Eq. (A.7). In this work, the linear system is solved by LU-decomposition followed by back substitution [Golub and Van Loan, 1996]. An advantage of this decomposition is that it need only be performed once for studies involving variations of boundary heat flux and/or boundary temperature.

Figure A.1. Typical discretization of a three-dimensional cubical region. The three visible sides of the cubical region have been discretized into a total of six triangular elements, each with a nodal point shown as a darkened point. One triangular element on the top of the cube is highlighted by a darkened perimeter. [Gelbard, 2001]

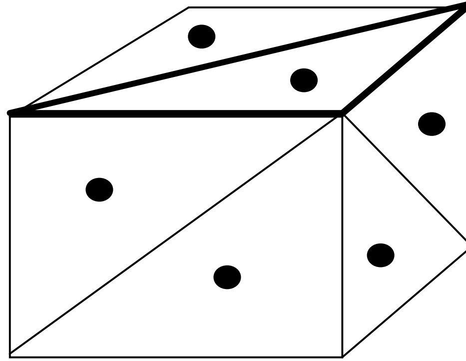

Once the boundary values are determined, the temperature at any point within the region V is then given by the discretized form of Eq. (A.6) as

$$T(\vec{r}) = \sum_{j=1}^{N} \left(\nabla' T(\vec{r}') \bullet \vec{n}'\right)_j \int_{S_j} G\left(\left|\vec{r} - \vec{r}'\right|\right) dS' - \sum_{j=1}^{N} T_j \int_{S_j} \nabla' G\left(\left|\vec{r} - \vec{r}'\right|\right) \bullet \vec{n}'\, dS', \qquad \text{(A.8)}$$

where $\vec{r}$ is in V but not on S.

There are several techniques for evaluating the integrals in Eqs. (A.7) and (A.8). In this work, an adaptive Gauss-Legendre algorithm [Kane, 1993] is used for triangles at arbitrary orientations as shown in Fig A.2. The triangular points are arbitrarily labeled 1, 2, and 3 in the Figure. The x- , y- and z-coordinates of point i are given by x_i, y_i, and z_i, respectively. Let L_1 and L_2 be the lengths from point 3 to point 1 and from point 3 to point 2, respectively. Thus

$$L_1 = \sqrt{(x_1 - x_3)^2 + (y_1 - y_3)^2 + (z_1 - z_3)^2} \tag{A.9}$$

Figure A.2. Diagram of triangular region at an arbitrary orientation relative to a fixed coordinate origin. The triangular points are labeled 1, 2, and 3. The natural coordinates from point 3 to points 1 and 2, are η_1 and η_2, respectively [Brebbia et al., 1984, p. 133].

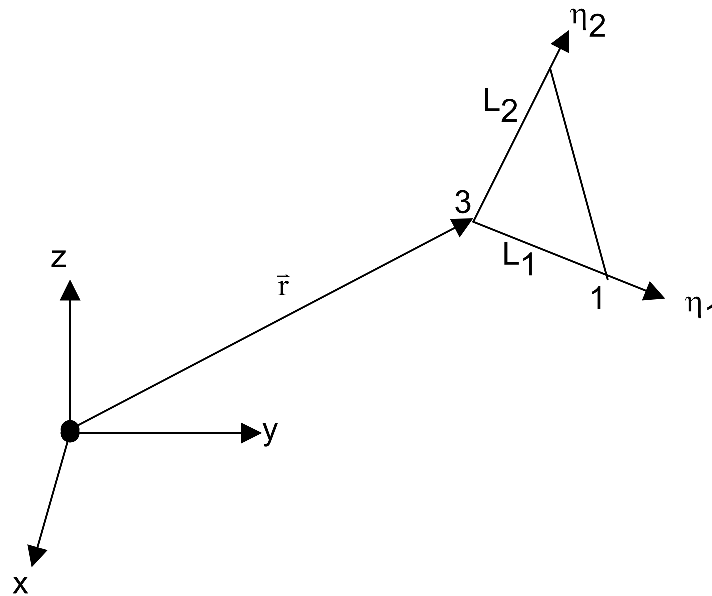

and

$$L_2 = \sqrt{(x_2 - x_3)^2 + (y_2 - y_3)^2 + (z_2 - z_3)^2} \tag{A.10}$$

The natural coordinates, η_1 and η_2 shown in Fig. A.2 are the dimensionless lengths along two of the legs of the triangle, defined as the length from point 3 to point 1 and from point 3 to point 2, respectively, divided by L_1 and L_2, respectively. Thus $0 \leq \eta_1 \leq$

1, $0 \le \eta_2 \le 1$, and $0 \le \eta_1 + \eta_2 \le 1$. A point (x, y, z) in the triangle can be expressed in terms of the triangular points and the natural coordinates η_1 and η_2, and is given by

$$x = \eta_1 x_1 + \eta_2 x_2 + (1-\eta_1-\eta_2)x_3, \tag{A.11}$$

$$y = \eta_1 y_1 + \eta_2 y_2 + (1-\eta_1-\eta_2)y_3, \text{ and} \tag{A.12}$$

$$z = \eta_1 z_1 + \eta_2 z_2 + (1-\eta_1-\eta_2)z_3. \tag{A.13}$$

In this work, the nodal point of the triangle is taken at $\eta_1 = \eta_2 = 1/3$, and the apex of an isosceles triangle is taken as point 3. The position of a point in the triangle with respect to a fixed origin is given by

$$\begin{aligned} \vec{r} = &\left[x_3 + (x_1 - x_3)\eta_1 + (x_2 - x_3)\eta_2\right]\hat{a}_x + \\ &\left[y_3 + (y_1 - y_3)\eta_1 + (y_2 - y_3)\eta_2\right]\hat{a}_y + \\ &\left[z_3 + (z_1 - z_3)\eta_1 + (z_2 - z_3)\eta_2\right]\hat{a}_z \end{aligned} \tag{A.14}$$

where are $\hat{a}_x, \hat{a}_y, \text{and } \hat{a}_z$ are the unit vectors in the x, y, z directions, respectively. In Fig. A.2 $\vec{r}$ is positioned at point 3 at which η_1 and η_2 are both zero. A Gauss-Legendre approximation of the integral of a function F over the triangle is then given by

$$I \approx A \sum_{k=1}^{N} F\left(\eta_1^{(k)}, \eta_2^{(k)}\right) w^{(k)} \tag{A.15}$$

where A is the area of the triangle, and the quadrature points $\eta_j^{(k)}$ (j = 1, 2) and weight factors $w^{(k)}$ are given in Kane [1993, p. 355] for N = 1, 3, 7, and 13. For convenience, these are also given in Table A.2. With the natural coordinate values from the Table A.2. The coordinate values x, y, and z can be determined from Eqs. (A.11), (A.12), and (A.13) such that the function F can be evaluated.

Table A.2. Quadrature points and weight factors for numerical integration of a function over a triangle [Kane, 1993, p. 355; Strang and Fix, 1973, p. 184].

N, k	$\eta_1^{(k)}$	$\eta_2^{(k)}$	w(k)
1, 1	1/3	1/3	1
3, 1	0.5	0.5	1/3
3, 2	0	0.5	1/3
3, 3	0.5	0	1/3
7, 1	1/3	1/3	0.25503 30000 30000
7, 2	0.79742 69853 53087	0.10128 65073 23456	0.12593 91805 44827
7, 3	0.10128 65073 23456	0.79742 69853 53087	0.12593 91805 44827
7, 4	0.10128 65073 23456	0.10128 65073 23456	0.12593 91805 44827
7, 5	0.05971 58717 89770	0.47014 20641 05115	0.13239 41527 88506
7, 6	0.47014 20641 05115	0.05971 58717 89770	0.13239 41527 88506
7, 7	0.47014 20641 05115	0.47014 20641 05115	0.13239 41527 88506
13, 1	0.06513 01029 02216	0.06513 01029 02216	0.05334 72356 08839
13, 2	0.86972 97941 95568	0.06513 01029 02216	0.05334 72356 08839
13, 3	0.06513 01029 02216	0.86972 97941 95568	0.05334 72356 08839
13, 4	0.31286 54960 04875	0.04869 03154 25316	0.07711 37608 90257
13, 5	0.63844 41885 69809	0.31286 54960 04875	0.07711 37608 90257
13, 6	0.04869 03154 25316	0.63844 41885 69809	0.07711 37608 90257
13, 7	0.63844 41885 69809	0.04869 03154 25316	0.07711 37608 90257
13, 8	0.31286 54960 04875	0.63844 41885 69809	0.07711 37608 90257
13, 9	0.04869 03154 25316	0.31286 54960 04875	0.07711 37608 90257
13, 10	0.26034 59660 79038	0.26034 59660 79038	0.17561 52574 33204
13, 11	0.47930 80678 41923	0.26034 59660 79038	0.17561 52574 33204
13, 12	0.26034 59660 79038	0.47930 80678 41923	0.17561 52574 33204
13, 13	0.33333 33333 33333	0.33333 33333 33333	-0.14957 00444 67670

For a flat surface that contains the point $\vec{r}_i$, $\nabla' G(|\vec{r}_i - \vec{r}'|) \bullet \vec{n}' = 0$. Thus in the summation on the left side of Eq. (A.7), for j = i the term is zero. Therefore, these integrals are zero and need not be calculated. In addition, a useful check on the accuracy of the integration procedure can be developed from the special case of T = 1 throughout V. In this case the temperature gradient is zero everywhere, and therefore Eq. (A.7) reduces to [Kane, p. 85, 1993]

$$\sum_{j=1}^{N} \int_{S_j} \nabla' G(|\vec{r}_i - \vec{r}'|) \bullet \vec{n}' \, dS' = -\frac{1}{2}. \qquad \text{(A.16)}$$

Notice that Eq. (A.16) is dependent only on the geometry, and completely independent of the temperature field. Therefore, Eq. (A.16) can be used for any temperature field as a set of N checks on the integration procedure for each element i = 1, ..., N. Alternatively, one may use Eq. (A.16) to “adjust” or scale the integrals such that Eq. (A.16) is satisfied exactly. We chose instead not to mask numerical approximation errors, and we use Eq. (A.16) for error analysis. Similarly, by conservation of energy, the sum of the net heat flux for all boundary elements must be zero. Instead of “adjusting” the individual element heat fluxes to satisfy this constraint, we use the error of a nonzero total net heat flux as a measure of the accuracy of the results. For all our calculations, this error is typically less than 0.4%.

The Gauss-Legendre algorithm, however, is inappropriate for evaluating integrable singularities, such as on the right-hand-side of Eq. (A.7) when i = j. In this case the Green’s function is singular when $\left|\vec{r}_i - \vec{r}'\right| = 0$. This singularity is integrable, and furthermore, is exactly analytically integrable over a triangular surface for the typical discretization used in this work. This can be shown by considering integration over a triangle shown in Figure A.3 in which the nodal point of the triangle is a darkened point. The integral is over the same element with the singularity. Because the integrand and limits of integration are expressed in terms of distance from the singularity, the location of the element in three-dimensional space is irrelevant. This triangle can be divided into three subtriangles, as shown in the Figure.

Figure A.3. The nodal point is shown as a darkened point in the center of the triangle. One of the three subtriangles is shown in which θ varies from 0 to θ_{max}. $R(\theta=0) = R_1$ and $R(\theta=\theta_{max}) = R_2$.

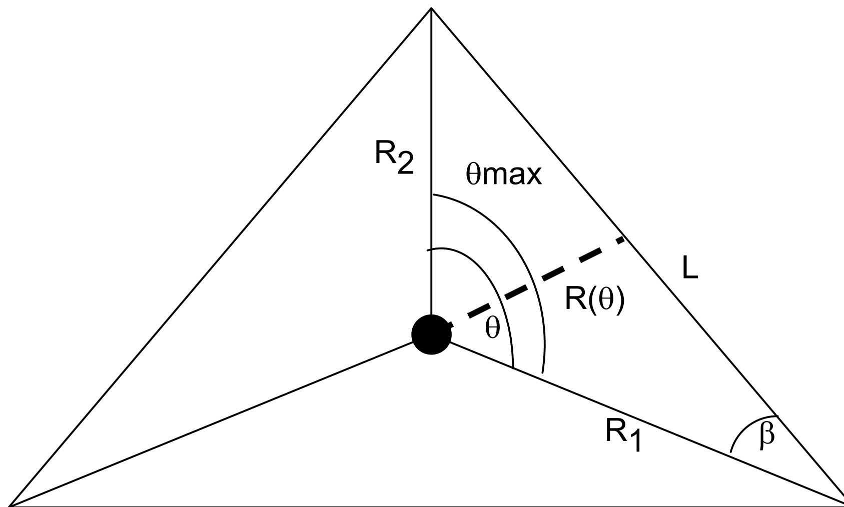

For the upper right sub triangle, $R(\theta)$ is shown as a dashed line and varies from R_1 to $R_2 = R(\theta_{max})$. By the law of cosines [Selby, 1973, p. 8]

$$\theta_{max} = \cos^{-1}\left[\frac{R_1^2 + R_2^2 - L^2}{2R_1R_2}\right] \tag{A.17}$$

and

$$\beta = \cos^{-1}\left[\frac{R_1^2 + L^2 - R_2^2}{2R_1L}\right]. \tag{A.18}$$

where the functional form for $R(\theta)$ is dependent on the angle β shown in Figure A.3, and by geometry $R(\theta)$ is given by

$$R(\theta) = \begin{cases} \dfrac{R_1}{\cos(\theta) + \dfrac{\sin(\theta)}{\tan(\beta)}}, & \beta < \dfrac{\pi}{2} \\[2ex] \dfrac{R_1}{\cos(\theta)}, & \beta = \dfrac{\pi}{2}. \\[2ex] R_1 \cos(\theta)\left[1 - \dfrac{\tan(\theta)}{\tan(\theta+\beta)}\right], & \beta > \dfrac{\pi}{2} \end{cases} \tag{A.19}$$

The integral on the right-hand-side of Eq. (A.7) over this subtriangle for $\beta < \pi/2$ is given by

$$\int_0^{\theta_{max}} \int_0^{R(\theta)} G\, r dr d\theta = \frac{1}{4\pi} \int_0^{\theta_{max}} \left[\frac{R_1}{\cos(\theta) + \dfrac{\sin(\theta)}{\tan(\beta)}}\right] d\theta, \qquad \left(\beta < \frac{\pi}{2}\right). \tag{A.20}$$

The integral on the right side of Eq. (A.20) can be integrated analytically [Selby, 1973], to give

$$\int_{0}^{\theta_{max}} \int_{0}^{R(\theta)} G\ r dr d\theta = \frac{R_1}{4\pi\sqrt{b^2+1}} \ln\left\{ \frac{\left[b - \sqrt{b^2+1} - \tan\left(\frac{\theta_{max}}{2}\right) \right]\left[b + \sqrt{b^2+1} \right]}{\left[b + \sqrt{b^2+1} - \tan\left(\frac{\theta_{max}}{2}\right) \right]\left[b - \sqrt{b^2+1} \right]} \right\}, \quad \left(\beta < \frac{\pi}{2}\right) \qquad \text{(A.21)}$$

where $b = 1/\tan(\beta)$.

For a general quadrilateral element in three-dimensional space, as shown in Figure A.5, we need to evaluate integrals of the form

$$\iint_{A_{element}} F(x, y, z) \quad dA \qquad \text{(A.22)}$$

where $A_{element}$ corresponds to the area of the element. This integral can be expressed in terms of two coordinates that are defined to reside in the plane of the element. Let these coordinates be ξ and η, be defined to range from –1 to +1 within the element. (The reasons for this definition of range will be explained shortly.)

Figure A.5. Quadrilateral element in three-dimensional space. The points are numbered sequentially 1 through 4. The coordinates in the plane of the element are ξ and η.

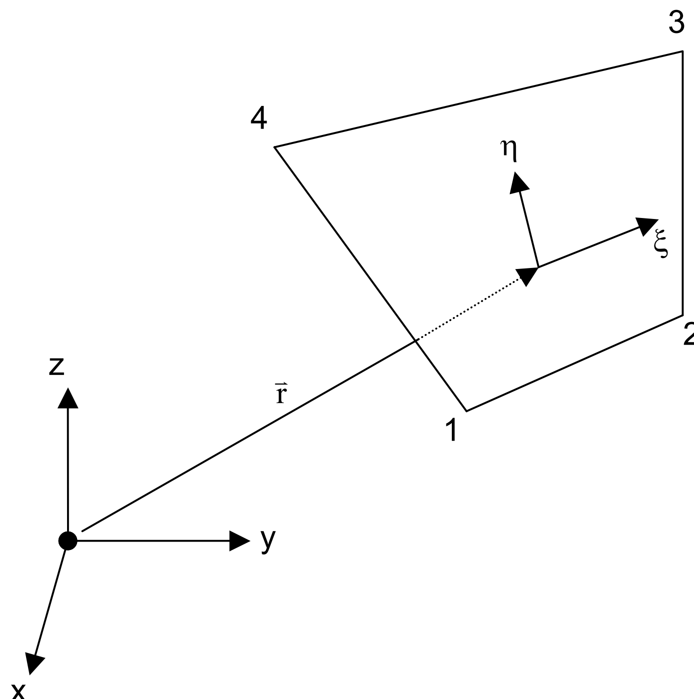

Let a vector from the origin to a position on the plane be given by

$$\vec{r} = x\hat{a}_x + y\hat{a}_y + z\hat{a}_z . \tag{A.23}$$

We select linear basis functions as (Strang and Fix, 1973)

$$\varphi_1 = \frac{1}{4}(1-\xi)(1-\eta) , \tag{A.24}$$

$$\varphi_2 = \frac{1}{4}(1+\xi)(1-\eta) , \tag{A.25}$$

$$\varphi_3 = \frac{1}{4}(1+\xi)(1+\eta) , \text{ and} \tag{A.26}$$

$$\varphi_4 = \frac{1}{4}(1-\xi)(1+\eta) \tag{A.27}$$

such that the spatial coordinates can be given by

$$x = x_1\varphi_1 + x_2\varphi_2 + x_3\varphi_3 + x_4\varphi_4, \tag{A.28}$$

$$y = y_1\varphi_1 + y_2\varphi_2 + y_3\varphi_3 + y_4\varphi_4, \text{ and} \tag{A.29}$$

$$z = z_1\varphi_1 + z_2\varphi_2 + z_3\varphi_3 + z_4\varphi_4. \tag{A.30}$$

Notice that because ξ and η range from –1 to +1, the linear basis functions φ_i are conveniently 1 at point i, and 0 at the other three points of the quadrilateral. It is for this reason that ξ and η were defined with this range.

A differential parallelogram in the plane of the element, with sides in the directions ξ and η has a differential area equal to the magnitude of the cross product of the differential lengths dr in the ξ and η directions. Thus

$$dA = \left| \frac{\partial \bar{r}}{\partial \xi} d\xi \times \frac{\partial \bar{r}}{\partial \eta} d\eta \right| = \left| \frac{\partial \bar{r}}{\partial \xi} \times \frac{\partial \bar{r}}{\partial \eta} \right| d\xi d\eta . \tag{A.31}$$

Because the normal to the surface of the differential parallelogram is given by the cross product of the partial derivatives of the position vector with respect to the two spatial coordinates,

$$\vec{n} = \frac{\partial \bar{r}}{\partial \xi} \times \frac{\partial \bar{r}}{\partial \eta} \tag{A.32}$$

and thus

$$dA = \left|\bar{n}\right| d\xi d\eta \,. \tag{A.33}$$

From this equation we see that the magnitude of the normal vector is the Jacobian for the transformation to integrate in the (ξ,η) coordinate system (Hildebrand, 1962, p. 347). For the linear basis functions

$$\begin{aligned}
\frac{\partial \bar{r}}{\partial \xi} &= \frac{\partial \bar{r}}{\partial x}\frac{\partial x}{\partial \xi} + \frac{\partial \bar{r}}{\partial y}\frac{\partial y}{\partial \xi} + \frac{\partial \bar{r}}{\partial z}\frac{\partial z}{\partial \xi} = \\
&+ \frac{1}{4}\left[(x_2 - x_1)(1-\eta) + (x_3 - x_4)(1+\eta)\right]\hat{a}_x \\
&+ \frac{1}{4}\left[(y_2 - y_1)(1-\eta) + (y_3 - y_4)(1+\eta)\right]\hat{a}_y \\
&+ \frac{1}{4}\left[(z_2 - z_1)(1-\eta) + (z_3 - z_4)(1+\eta)\right]\hat{a}_z
\end{aligned} \tag{A.34}$$

and

$$\begin{aligned}
\frac{\partial \bar{r}}{\partial \eta} &= \frac{\partial \bar{r}}{\partial x}\frac{\partial x}{\partial \eta} + \frac{\partial \bar{r}}{\partial y}\frac{\partial y}{\partial \eta} + \frac{\partial \bar{r}}{\partial z}\frac{\partial z}{\partial \eta} = \\
&+ \frac{1}{4}\left[(x_4 - x_1)(1-\xi) + (x_3 - x_2)(1+\xi)\right]\hat{a}_x \\
&+ \frac{1}{4}\left[(y_4 - y_1)(1-\xi) + (y_3 - y_2)(1+\xi)\right]\hat{a}_y \\
&+ \frac{1}{4}\left[(z_4 - z_1)(1-\xi) + (z_3 - z_2)(1+\xi)\right]\hat{a}_z
\end{aligned} \tag{A.35}$$

Substituting these expressions results in

$$16\vec{n} = \left\{ \begin{array}{l} \left[(y_2 - y_1)(1-\eta) + (y_3 - y_4)(1+\eta)\right]\left[(z_4 - z_1)(1-\xi) + (z_3 - z_2)(1+\xi)\right] \\ -\left[(z_2 - z_1)(1-\eta) + (z_3 - z_4)(1+\eta)\right]\left[(y_4 - y_1)(1-\xi) + (y_3 - y_2)(1+\xi)\right] \end{array} \right\} \hat{a}_x$$

$$+ \left\{ \begin{array}{l} \left[(z_2 - z_1)(1-\eta) + (z_3 - z_4)(1+\eta)\right]\left[(x_4 - x_1)(1-\xi) + (x_3 - x_2)(1+\xi)\right] \\ -\left[(x_2 - x_1)(1-\eta) + (x_3 - x_4)(1+\eta)\right]\left[(z_4 - z_1)(1-\xi) + (z_3 - z_2)(1+\xi)\right] \end{array} \right\} \hat{a}_y \quad \text{(A.36)}$$

$$+ \left\{ \begin{array}{l} \left[(x_2 - x_1)(1-\eta) + (x_3 - x_4)(1+\eta)\right]\left[(y_4 - y_1)(1-\xi) + (y_3 - y_2)(1+\xi)\right] \\ -\left[(y_2 - y_1)(1-\eta) + (y_3 - y_4)(1+\eta)\right]\left[(x_4 - x_1)(1-\xi) + (x_3 - x_2)(1+\xi)\right] \end{array} \right\} \hat{a}_z$$

This can be more compactly written as

$$\vec{n} = n_x \hat{a}_x + n_y \hat{a}_y + n_z \hat{a}_z \,. \qquad \text{(A.37)}$$

The Jacobian is then given by magnitude of the normal vector.

$$J = |\vec{n}| = \sqrt{n_x^2 + n_x^2 + n_x^2} \qquad \text{(A.38)}$$

and the integral of a function F over a quadrilateral element is given by,

$$\iint_{A_{element}} F(x,y,z) \quad dA = \int_{-1}^{+1} \int_{-1}^{+1} F[x(\xi,\eta), y(\xi,\eta), z(\xi,\eta)] \, J \, d\xi d\eta \,. \qquad \text{(A.39)}$$

The right-hand-side of Eq. (A. 39) can be evaluated using Gauss-Legendre quadrature for each direction. The algorithm is made adaptive by dividing the square domain into four quadrants and reapplying Gauss-Legendre quadrature to each quadrant. If the sum of the four integrals is equal (within specified tolerance limits), to the integral over the entire domain using only one application of Gauss-Legendre quadrature, then convergence has been achieved. If not, then each quadrant is further subdivided into quadrants and the same convergence check is performed. This process is repeated until convergence is achieved, or at most ten level of quartering has been achieved.

Appendix B: Process flow sheet for microTCD

For this process use a Silicon {100} n-type wafer with delft nitride on both sides of the wafer.

Notes for process sheet:
Standard solvent clean refers to cleaning the wafers with acetone, methanol and isopropanol (in that order), rinsing the wafers in water bath until the bath reaches resistivity and drying the wafers with the nitrogen gun. Water resistivity should be 18 MO, but 13 MO is sufficient.

Also please solvent clean masks before patterning the wafers. Inspect the mask under the microscope to make sure that there is no resist on them.

If you do a piranha clean, followed by an HF dip, please rinse the wafer(s) before putting into HF. Piranha is H_2SO_4:H_2O_2, usually a volumetric ratio of 7:3 or 4:1 (your choice). DO NOT CLEAN with piranha if wafers have metal on them!!

110_FIND Mask

Please obtain mask from Sara Sokolowski or from Ron Manginell.

_____1. CLEAN WAFER(S)

Use a standard solvent clean or a piranha clean with an HF dip.

_____2. Pattern Mask

_____a. Dehydration Bake and HMDS prime in vacuum prime oven.
_____b. Spin on AZ4330 on back of wafer at 4000 RPM for 30 sec.
_____c. Hard bake for about 5 minutes at 120 oC. To prevent contamination and dirtying of front side, please use two glass slides to place the wafer on.
_____d. Spin on AZ4330 on front side of wafer at 4000 RPM for 30 sec.
_____e. Hard bake for 90 seconds at 90 oC.
_____f. Align mask to flat on wafer.
_____g. Expose for 6.5 seconds.
_____h. Develop in MF 319 developer for 2.5 seconds or AZ400K 1:4 developer for about 1.5 minutes. Please watch wafer develop.
_____i. Rinse wafer to water resisitvity and dry with nitrogen gun.
_____j. Inspect under microscope

_____3. Plasma Descum in LFE

_____k. Descum for 3 minutes under 5 FWD WATT power

_____4. ETCH NITRIDE (use 790 Plasma Therm RIE or Vacutek)

_____a. Use following Recipe:

CF_4 40 sccm

O_2 2 sccm (should read 10 sccm in Vacutek)

Forward Power 100 W

Pressure 100 mTorr

Time: 25 minutes

NOTE: The time for this etch is in the Vacutek. 25 mintues will etch 1 m of LPCVD nitride. The etch rate in the Vacutek for Si_xN_y is ~400 A/min. If using the 790 Plasma Therm series RIE please look for an etch rate to figure out time, or calculate one. If there is a standard recipe for Si_xN_y please use standard recipe in 790.

_____b. Confirm nitride is gone using nanospec or ellipsometer.

_____5. REMOVE RESIST

_____c. Let wafer soak in Acetone for about 10 minutes.
_____d. Spray with acetone gone
_____e. Clean wafers with standard solvent clean.
_____f. Use Den's clean in LOLA for 30 minute.

_____6. KOH ETCH (use appropriate PPE)

Steps a and b should be done about 1 hour before the etch.

_____g. Turn on KOH nitrogen and water in CHASE.
_____h. Press power on, wait for thermometer to read room temperature, press Heat ON.
_____i. Once bath has reached 85 ^{o}C place wafers in bath, make sure to use a TEFLON boat.
_____j. Etch for 15 minutes
_____k. Remove wafers from bath, rinse for 5-10 minutes.
_____l. Dry with nitrogen gun.

FINDING THE 110 PLANE

Here are some helpful notes on how to do it.

It is easiest to do this with the confocal microscope located next to the acid bench since it will not reverse the image.

Find this fork in the left or right side:

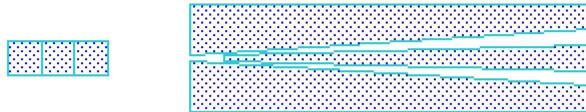

Zoom in to forks; see where the forks are the same length.
For example, you might see something like this:

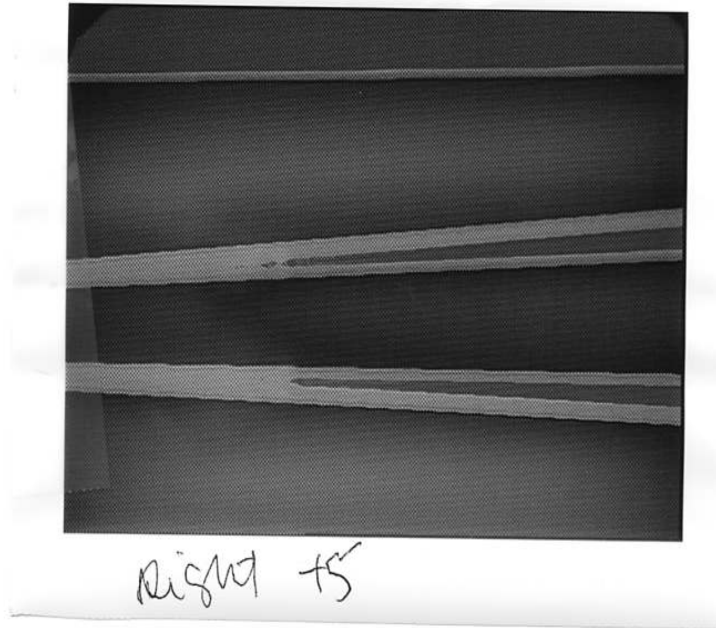

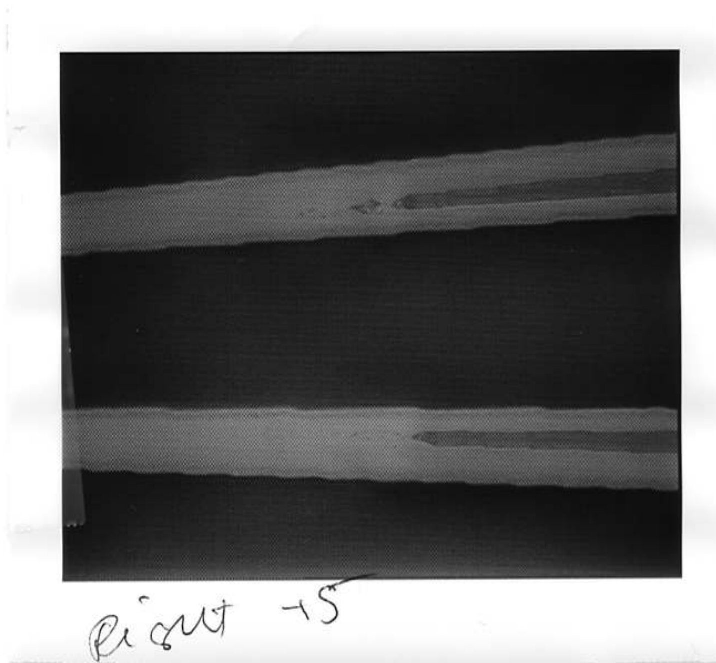

After you find the fork which is the same length, make sure to count its location from the centerAway from the flat is denoted as +, towards the flat is denoted as -.

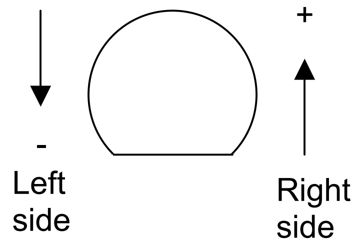

Also the number of forks should be the same, but in opposite direction in the left and right side of the wafer. So, if you have +5 on the right, you should have –5 on the left. But make sure to count forks on both sides. Also the direction on the left or right is not always the same, you can have –5 on the right and +5 on the left.

METAL 1 MASK

In this part you will align the metal mask according to where you found the 110 plane.

For example, you found that the 110 plane is +5 on the right side. So you need to move +10 when aligning since you will hold one side at 0.

0 is where there is one major hole and two smaller ones:

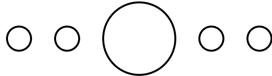

So you would stay at 0 on the left side and move 10 circles away from the right side.

_____7. CLEAN WAFER(S)

Use a standard solvent clean or a piranha clean with an HF dip.

_____8. Pattern wafer with Mask

_____m. Dehydration Bake and HMDS prime in vacuum prime oven
_____n. Spin on JSR at 3000 RPM for 30 sec.
_____o. Hard bake for 1 minute at 120 ^{o}C.
_____p. Align wafer to mask.
_____q. Expose for 4 seconds.
_____r. **POST BAKE** for 45 sec at 100 oC.
_____s. Develop with AZ400K 1:4 developer for about 1 minute. Please watch wafer develop.
_____t. Rinse wafer to water resisitvity and dry with nitrogen gun.
_____u. Inspect under microscope

_____9. Plasma Descum in LFE

_____v. Descum for 3 minutes under 5 FWD WATT power

_____10. Resistor/heater metalization

_____w. Make sure to have correct metals in targets
_____x. Load sample
_____y. Sputter Cr and Pt using the following parameters, for tooling factors use current tooling factors if available.

Cr (200 A)
Pressure 10 mTorr
Power 200 W
Tooling 150

Pt (5000 A)
Pressure 10 mTorr
Power 185
Tooling 185

_____z. Place wafers in acetone for liftoff. (make sure to cover and let soak for hours until metal lifts).

_____aa. Spray wafer with acetone gun

_____bb. Inspect wafer under microscope (repeat spray if needed)

_____cc. Solvent clean wafers

_____dd. Measure metal thickness using Dektak

_____11. CLEAN WAFERS WITH DEN'S CLEAN in LOLA

_____12. Anneal metal

_____ee. Place wafers in 6" tube furnace and anneal for 30 minutes at 500 ^{o}C.

METAL 2 MASK

_____1. Clean wafers

_____2. Pattern wafer with metal 2 Mask

_____ff. Dehydration bake and HMDS prime in vacuum prime oven.

_____gg. Spin on JSR at 3000 RPM for 30 sec.

_____hh. Hard bake for 1 minute at 120 oC

_____ii. Align Mask. (align to flat, align globals and vernier alignment marks)

_____jj. POST BAKE for 45 sec at 100 oC

_____kk. Develop with AZ400K 1:4 developer, watch wafer develop

_____ll. Rinse to water resistivity

_____mm. I
nspect under microscope

_____3. Plasma Descum in LFE

_____nn. Descum for 3 minutes under 5 FWD WATT power

_____4. Bond pad metalization

_____oo. Evaporate Cr/Au in EG1 or EG3

_____pp. Place wafers in acetone for liftoff. (make sure to cover and let soak for hours until metal lifts).

_____qq. Spray wafer with acetone gun

_____rr. Inspect wafer under microscope (repeat spray if needed)

_____ss. Solvent clean wafers

_____tt. Measure metal thickness using Dektak

_____5. CLEAN WAFERS WITH DEN'S CLEAN in LOLA

KOH Mask

_____6. Pattern Mask

_____uu. Dehydration Bake and HMDS prime in vacuum prime oven.

_____vv. Spin on AZ4330 on back of wafer at 4000 RPM for 30 sec.

_____ww. H
ard bake for about 5 minutes at 120 oC. To prevent contamination and dirtying of front side, please use two glass slides to place the wafer on.

_____xx. Spin on AZ4330 on front side of wafer at 4000 RPM for 30 sec.

_____yy. Hard bake for 90 seconds at 90 oC.

_____zz. Align mask, you must use the metal squares on the left and right side of the wafer as the alignment features. (These are the squares surrounding the target to the 110 find circles). After you are aligned look to make sure no resistors show through trapezoids.

_____aaa. E
xpose for 6.5 seconds.

_____bbb. D
evelop in MF 319 developer for 2.5 seconds or AZ400K 1:4 developer for about 1.5 minutes. Please watch wafer develop.

_____ccc. R
inse wafer to water resisitvity and dry with nitrogen gun.

_____ddd. I
nspect under microscope

_____7. Plasma Descum in LFE

_____eee. D
escum for 3 minutes under 5 FWD WATT power

_____8. ETCH NITRIDE (use 790 Plasma Therm RIE or Vacutek)

_____fff. Use following Recipe:

CF_4 40 sccm
O_2 2 sccm (should read 10 sccm in Vacutek)
Forward Power 100 W
Pressure 100 mTorr
Time: 25 minutes

NOTE: The time for the etch is in the Vacutek. 25 mintues will etch 1   m of LPCVD nitride. The etch rate in the Vacutek for Si_xN_y is ~400 A/min. If using the 790 Plasma Therm series RIE please look for an etch rate to figure out time, or calculate one. If there is a standard recipe for Si_xN_y please use standard recipe in 790.

_____ggg. C
onfirm nitride is gone using nanospec or ellipsometer.

_____9. REMOVE RESIST

_____hhh. L
et wafer soak in Acetone for about 10 minutes.

_____iii. Spray with acetone gone

_____jjj. Clean wafers with standard solvent clean.

_____kkk. U
se Den's clean in LOLA for 30 minute.

_____10. KOH ETCH (use appropriate PPE)

Steps a and b should be done about 1 hour before the etch.

_____lll. Turn on KOH nitrogen and water in CHASE.

_____mmm.
Press power on, wait for thermometer to read room temperature, press Heat ON.

_____nnn. O
nce bath has reached 85 ^{o}C place wafers in bath, make sure to use a TEFLON boat.

_____ooo. E
tch for 1 hour, inspect with confocal microscope get etch rate. Put back in bath for approximately 4.5 hours until etched through.

_____ppp. R
emove wafers from bath, rinse for 5-10 minutes.

_____qqq. D
ry with nitrogen gun.

The devices are located as follows:

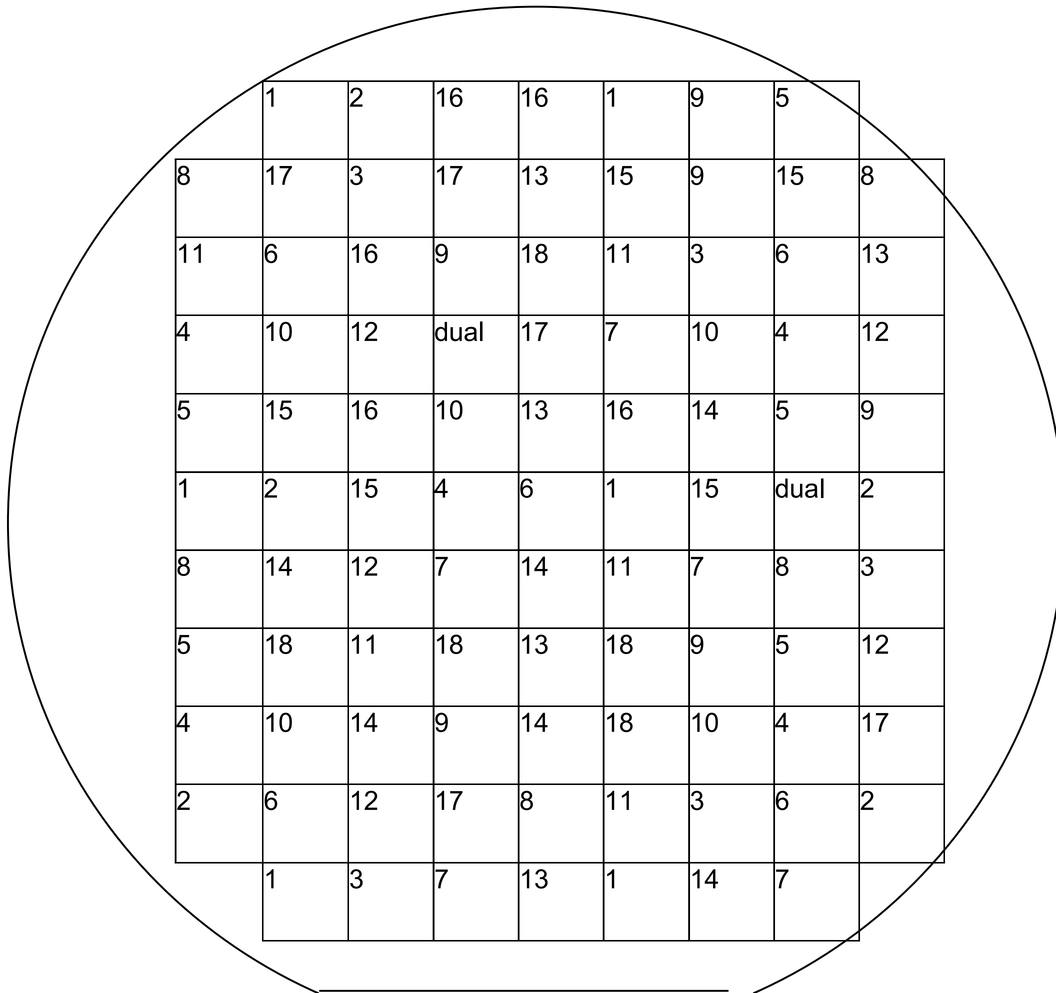

The numbers represent the following devices:

Number	Membrane L (um)	Trapezoid height (um)	Flow type
1	100	100	Parallel
2	100	200	Parallel
3	100	300	Parallel
4	200	100	Parallel
5	200	200	Parallel
6	300	100	Parallel
7	300	200	Parallel
8	400	100	Parallel
9	500	100	Parallel
10	100	100	Perpendicular
11	100	200	Perpendicular
12	100	300	Perpendicular
13	200	100	Perpendicular
14	200	200	Perpendicular
15	300	100	Perpendicular
16	300	200	Perpendicular
17	400	100	Perpendicular
18	500	100	Perpendicular

Figure 43 Schematic of needed changes to the standard μChemLab electronics board to support the thermal conductivity detector.

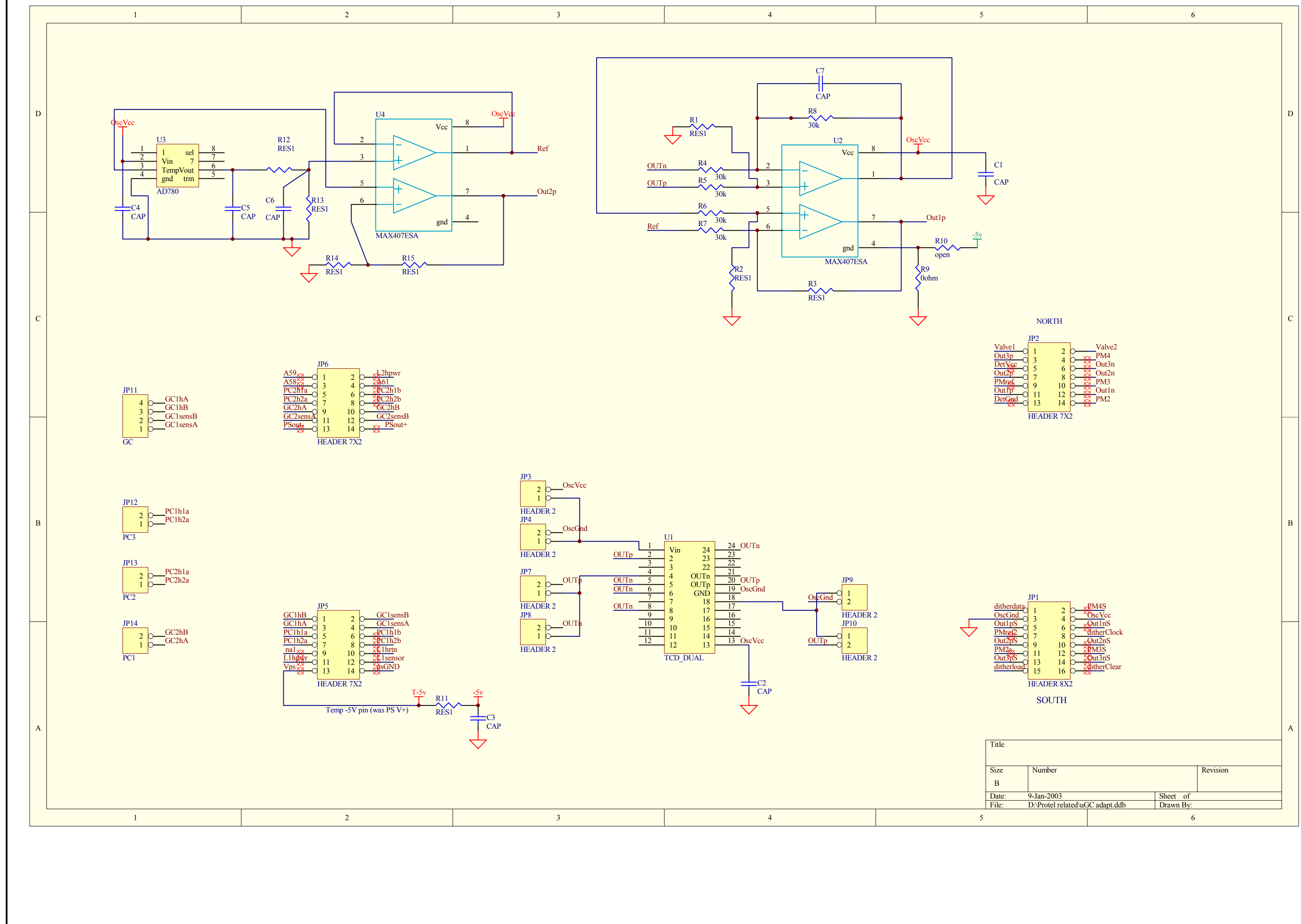

References

Arfken, G., *Mathematical Methods for Physicists*, 3rd Edition, Academic Press, Florida, 1985.
Brebbia, C. A., J. C. F. Telles, and L. C. Wrobel, *Boundary Element Techniques: Theory and Applications in Engineering*, Springer, New York, 1984.
Brebbia, C. A. and J. Dominguez, *Boundary Elements: An Introductory Course, 2nd Ed*, McGraw-Hill, New York, 1992.
Chen, K. and Wu, Y., "Thermal analysis and simulation of the microchannel flow in miniature thermal conductivity detectors," *Sensors and Actuators A,* 79, 211-218, 2000.
CRC Handbook of Chemistry and Physics (3rd Electronic Edition)
Gajda, M. A. and Ahmed, H., "Applications of thermal silicon sensors on membranes," *Sensors and Actuators,* A 49, 1-9, 1995.
Gelbard, F., *Modeling the Electronic States of Quantum Structures*, Ph.D. Thesis, University of New Mexico, Albuquerque, New Mexico, May 2001.
Gelbard, F. and K. J. Malloy, "Modeling Quantum Structures with the Boundary Element Method," *J. Computational Physics*, 172, 19-39, 2001.
Golub, G. H. and C. F. Van Loan, *Matrix Computations*, 3rd Edition, Johns Hopkins University Press, Baltimore, Maryland, 1996.
Grob, R. L. (Editor), Modern Practice of Gas Chromatography, 3rd Edition, Wiley Interscience, New York, 1995.
Hildebrand, F. B., *Advanced Calculus for Engineers*, Prentice-Hall, Englewood Cliffs, New Jersey, 1962.
Kane, J. H., *Boundary Element Analysis in Engineering Continuum Mechanics*, Prentice Hall, Englewood Cliffs, New Jersey, 1993.
Kimura, M., Manaka, J., Sato, S., Takano, S., Igarashi, N., and Nagai, K., " Application of the air-bridge microheater to gas detection." *Sensors and Actuators B*, 24-25, 857-860, 1995
Kovacs, G. T. A., Micromachined Transducers Sourcebook, McGraw-Hill, San Francisco, 1998.
Laugere, F., Lubking, G.W., Berthold, A., Bastemeijer, J., and Vellekoop, M. J., "Downscaling aspects of a conductivity detector for application in on-chip capillary electrophoresis." *Sensors and Actuators A*, 92, 109-114, 2001
Madou, M., Fundamentals of Microfabrication. Chemical Rubber Company Press, Florida, 2001.
Muto, H. *US Patent 5756878*, May 26, 1998.
Selby, S. M. (Ed.) *Standard Mathematical Tables*, 21st Ed., The Chemical Rubber Co., Cleveland, Ohio, 1973.
Simon, I. and Arndt, M., "Thermal and gas-sensing properties of a micromachined thermal conductivity sensor for the detection of hydrogen in automotive applications." *Sensors and Actuators A*, 97-98, 104-108, 2002
Sitteler, F. C. *US Patent 4909078*, Mar. 20, 1990.
Sorge, S. and Pechstein, T., "Fully integrated thermal conductivity sensor for gas chromatography without dead volume." *Sensors and Actuators A*, 63, 191-195, 1997

Strang, G. and Fix, G. J., *An Analysis of the Finite Element Method*, Prentice-Hall, Englewood Cliffs, New Jersey, 1973.
Varian website: www.varianc.com
Wu, Y. E., Chen, K., Chen, C. W., and Hsu, K. H., "Fabrication and characterization of thermal conductivity detectors (TCDs) of different flow channel and heater designs." *Sensors and Actuators B*, 100, 37-45, 2002

Distribution

5	MS0892	Steven Showalter, 1764
1	MS0630	Dolores Cruz, 1764
1	MS0630	Ron Manginell, 1764
1	MS0892	Richard Kottenstette, 1764
1	MS0892	Douglas Adkins, 1764
1	MS0748	Fred Gelbard, 6415
1	MS1073	George Dulleck, 1738
4	MS0755	Wayne Einfeld, 6233
1	MS0755	Daniel Horschel, 6233
1	MS1127	K. Scott Rawlinson, 6218
1	MS0892	Richard Cernosek, 1764
1	MS1425	Alex Robinson, 1764
1	MS0188	Donna Chavez, LDRD Office, 1011
1	MS 0918	Central Technical Files, 8945-1
2	MS0899	Technical Library, 9616
1	MS0612	Review and Approval Desk, 9612 for DOE/OSTI